FISEVIER

Contents lists available at ScienceDirect

## Journal of Sound and Vibration

journal homepage: www.elsevier.com/locate/jsvi





# Revisiting the frozen gust assumption through the aeroacoustic scattering of wavepackets by a semi-infinite plate

Sonya Tiomkin \*,1, Justin W. Jaworski<sup>2</sup>

Department of Mechanical Engineering and Mechanics, Lehigh University, Bethlehem, PA 18015, USA

#### ARTICLE INFO

Keywords: Wavepacket Trailing-edge noise Frozen gust assumption

#### ABSTRACT

This paper presents an analytic solution for the aerodynamic noise generated by a traveling wavepacket passing near the edge of a rigid semi-infinite flat plate. The solution is derived in the time domain for a wavepacket of either constant or spatially-varying wavenumber, for which novel closed-form expressions are obtained for the incident and scattered sound fields. The case of a varying wavepacket constitutes a surrogate model for turbulent flow distortions caused by the edge region and its geometry. This modeling approach permits a relaxation of the frozen gust assumption that is commonly used in the analytical prediction of trailing-edge noise, whereby the local vorticity is assumed to be unaffected by the edge. Our results shed light on the role that spatial variations of the vortical field near the trailing edge have on the incident and scattered sound contributions to the acoustic far field. In particular, we find that the wavenumber modification has a significant effect on the incident field but not on the scattered field amplitude. However, the phase difference between the incident and scattered fields depends strongly on the spatial variation in the wavepacket wavenumber, which leads to a variation in the sound level and directivity of the total pressure field.

#### 1. Introduction

The constant growth of air traffic volume and the encroachment of major airports on their neighboring communities have recently led to more stringent regulations for aircraft noise [1]. Noise regulations are also a major factor in the future of efficient urban air transportation [2]. Thus, there is an accelerating scientific interest in the reduction of aerodynamic noise from air vehicles.

One of the predominant sources of aerodynamic airframe noise is the interaction of turbulence with the wing trailing edge, known as trailing-edge noise [3]. A common approach to suppress this noise is the use of serrated trailing edges, which are geometric waveforms that run periodically along the wing span, as may be inspired by the wings of silent owl species [4,5]. This mechanism has been shown to be effective in numerous theoretical [6–8], computational [9,10], and experimental [11] studies. However, there is currently poor agreement between predictive theory and computational and experimental results, accompanied by an incomplete understanding of the mechanism by which serrations alter aerodynamic noise.

The standard aeroacoustic theory for serrated trailing edges by Howe [6,7] is based upon the 'frozen gust' assumption, which assumes that the vorticity in the turbulent boundary layer is unaffected by the presence of the trailing edge. This theory overestimates the noise reduction measured in practice for serrated trailing edges by 2 to 5 dB on average [11], in contrast to trailing-edge noise theory for *straight* edges for which very good agreement with measurements is observed [12]. Recent studies [8,10] infer that these

E-mail addresses: sonyat1@usf.edu (S. Tiomkin), jaworski@vt.edu (J.W. Jaworski).

<sup>\*</sup> Corresponding author.

<sup>&</sup>lt;sup>1</sup> Current address: Department of Mechanical Engineering, University of South Florida, Tampa, FL 33620, USA.

<sup>&</sup>lt;sup>2</sup> Current address: Department of Aerospace and Ocean Engineering, Virginia Tech, Blacksburg, VA 24060, USA.

discrepancies are due to the local effect that the serrated edge has on the turbulent field, in violation of the frozen gust assumption. For example, the experimental velocity- and acoustic-field measurements presented by Moreau and Doolan [9] for a flat plate with either a straight or serrated trailing edge show that the serrated edge has a significant influence on the hydrodynamic field at the source location, which strongly affects the acoustic emission from the edge. Avallone et al. [10,13] confirmed this conclusion by computational analysis and experimental measurements, respectively. The particle image velocimetry measurements that Avallone et al. [13] present on the suction side of the serrated trailing edge identify counter-rotating streamwise-oriented vortical structures that distort the wake flow near the edge. This complex flow pattern in the wake is hypothesized to be responsible for the reduced effectiveness of trailing-edge serrations for noise suppression, as compared to available predictive theory [14]. More details on the effect of trailing edge geometry on the surrounding flow and its effect on the radiated sound can be found in the recent review of Lee et al. [14].

The present research seeks to investigate the above hypothesis by incorporating spatial distortions of the vorticity field into a noise prediction model. This goal is pursued by developing an analytical model to predict the noise from the encounter of a traveling wavepacket with the edge of a semi-infinite flat plate.

The study of noise produced by a *static* wavepacket originates from Crow [15]. Crow used a simplified one-dimensional wavepacket model to describe the Lighthill stress tensor, and applied it to the Lighthill integral to predict the sound generated by the wavepacket (see also details in Crighton [16]). This wavepacket model represented the pressure fluctuations outside of a turbulent jet, which led to the identification of an exponential polar variation in the resulting sound pressure, referred to as superdirectivity [17]. Crighton and Huerre [17] showed in their theoretical analysis that this superdirectivity is only obtained for non-compact wavepackets that are characterized by  $k_h L_1 \gg 1$ , where  $k_h$  is the convected wavenumber and  $L_1$  is the characteristic length scale (standard deviation) of the Gaussian envelope of the wavepacket. The superdirectivity phenomenon was confirmed experimentally by Cavalieri et al. [18] for the axisymmetric mode of the acoustic pressure in subsonic jets; these authors also validated the use of the line source approximation suggested by Crow [15] for sound pressure prediction.

Recent research by Cavalieri et al. [19] and Nogueira et al. [20] focuses on the sound produced by a wavepacket source near the edge of a flat plate, as motivated by the study of sound generation from an exhaust jet installed near an aircraft wing. In particular, Cavalieri et al. [19] combine experimental measurements and two different numerical analyses to study the effect of the distance between a wavepacket representing the jet turbulence and the plate edge on the scattered sound. Their first numerical solution uses the method of Ffowcs Williams and Hall [21] to predict wavepacket scattering by a semi-infinite plate edge, while their second numerical approach, using a boundary element method accelerated by a fast multipole method [22], predicts the sound scattered from a finite plate. The results from both approaches show an exponential dependence of the radiated sound on the jet-plate distance, in agreement with their experiments. However, for all of the considered cases, the sound pressure levels (SPL) predicted by the numerical results of Cavalieri et al. [19] were slightly lower than experimental measurements, a difference which may be due to the fact that the source model comprises only the axisymmetric mode of the jet. Both numerical approaches in Cavalieri et al. [19] show that the sound field radiated by the jet-wing interaction presents a low-frequency amplification with dipolar directivity. As expected, the directivity pattern of their finite-plate solution has additional waviness when compared against the semi-infinite plate results, which is due to secondary scattering from the leading and lateral edges of the plate and the interference of scattered sound from several edges in the acoustic far field (e.g., Cavalieri et al. [23] and Ayton et al. [24]). Nogueira et al. [20] further simplifies the volume wavepacket source used by Cavalieri et al. [19] by assuming a wavepacket that is concentrated on a cylindrical surface following the jet lipline. The good agreement between the results of Nogueira et al. [20], obtained using the tailored Green's function of Ffowcs Williams and Hall [21], and the results that Cavalieri et al. [19] present for a semi-infinite plate shows that this simplification in the wavepacket model has very little effect on the computed sound.

The current study extends the line-source wavepacket model suggested by Crow [15] to examine the noise produced by a *traveling* wavepacket that moves along the surface of a rigid flat plate. This problem is solved analytically in the time domain to allow for spatial variation in the convected wavenumber of the wavepacket, in contrast to the usual approach in the frequency domain that describes the solution for a constant wavenumber (e.g., Cavalieri et al. [19]). In effect, the wavepacket with spatial wavenumber variations is a surrogate model for turbulent flow distortions created by real flows near a trailing edge. Novel closed-form expressions are obtained for the incident and scattered pressure fields due to the encounter of the wavepacket with the plate edge, which are verified against previous numerical results by Cavalieri et al. [19] for a static wavepacket of constant wavenumber. In addition, the effect of the wavenumber spatial distortion is studied, shedding light on the role that distortions in the vorticity field due to trailing edge geometry could have in the trailing-edge noise mechanism.

The remainder of this paper is organized as follows. Section 2 presents the mathematical formulation of the problem and the general approach to the solution. The analytical solution is derived in Section 3, and the results of the theoretical model and their implications are presented and discussed in Section 4. Section 5 closes with concluding remarks.

## 2. Mathematical model

The mathematical approach in this study considers the incident and scattered pressure fields separately and then superimposes these fields to obtain the total aerodynamic noise produced by an encounter of a moving wavepacket with the edge of a semi-infinite plate, as depicted in Fig. 1. The incident field is obtained from Lighthill's analogy in Section 2.1, and the scattered field is predicted by utilizing Green's theorem in Section 2.2.

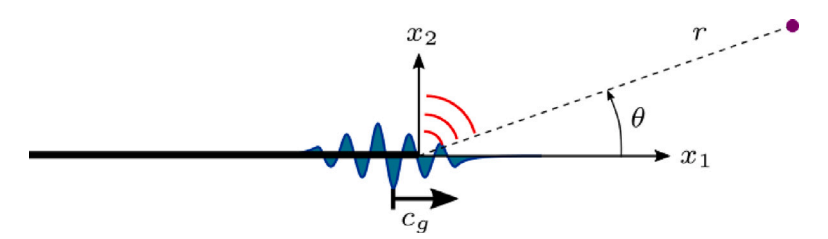


Fig. 1. Schematic description of the problem: a wavepacket travels along a semi-infinite plate with speed  $c_g$  and produces sound as it passes the plate edge. We focus on the sound that radiates to an observer in the acoustic far field at a radial distance r from the plate edge.

## 2.1. Incident field

Lighthill's analogy yields an expression for the far-field noise radiation in a free space (see Howe [25], pp. 25–29),

$$p_i(\mathbf{x},t) = \frac{1}{4\pi} \int_{-\infty}^{\infty} \left[ \frac{1}{|\mathbf{x} - \mathbf{y}|} \frac{\partial^2 T_{ij}(\mathbf{y}, \tau)}{\partial y_i \partial y_j} \right]_{\tau = t - \frac{|\mathbf{x} - \mathbf{y}|}{co}} d^3 \mathbf{y}, \tag{1}$$

where  $T_{ij}$  is the Lighthill stress tensor, x is the observer location, y is the sound source position,  $c_0$  is the speed of sound, and  $d^3y$  denotes volumetric integration of the source region. This method requires knowledge of the source term,  $T_{ij}$ , which may be obtained from computational fluid dynamics simulations or prescribed by a simplified model. The current study takes the latter approach and prescribes the form of  $T_{ij}$  to predict the incident sound produced by a moving wavepacket that can be expressed in closed form.

#### 2.2. Scattered field

The compact Green's function (e.g., Howe [25], Chap. 3) may be used to predict the sound scattered by a rigid boundary for problems where the wavelength of the produced sound is large compared to the dimensions of the solid body. Alternatively, this method can also be applied to the half-plane problem of Howe [26] when the acoustic wavelength is large compared to the distance between the source and the plane edge. We pursue the Green's function approach in the time domain, contrarily to the usual application of Green's functions in the frequency domain (e.g., Cavalieri et al. [19]), with the purpose of introducing a spatial variation to the turbulence source that cannot be analyzed in the frequency domain. These spatial distortions aim to represent the possible effect of trailing edge geometry on the vorticity field that scatters as noise. However, we note that here the spatially-varying turbulence source is scattered by a straight edge to focus solely on the effect of the vorticity change on the scattered pressure field.

The appropriate two-dimensional Green's function that satisfies the boundary conditions of the semi-infinite plate is (see Howe [25], p. 75)

$$G_{1_{2D}}(\bar{\mathbf{x}}, \bar{\mathbf{y}}, t - \tau) \cong \frac{\varphi^*(\bar{\mathbf{x}})\varphi^*(\bar{\mathbf{y}})}{\pi r} \delta\left(t - \tau - \frac{r}{c_0} + \frac{\tilde{\mathbf{x}} \cdot \bar{\mathbf{y}}}{c_0}\right),\tag{2}$$

where

$$\varphi^*(\bar{\mathbf{x}}) = \sqrt{r} \sin \frac{\theta}{2},\tag{3}$$

 $\bar{x} = (x_1, x_2) = (r\cos\theta, r\sin\theta), \ \bar{y} = (y_1, y_2) = (r_0\cos\theta_0, r_0\sin\theta_0), \ \text{and} \ \tilde{x} = \bar{x}/r.$  See the coordinate definitions of  $r, \theta$  in the schematic drawing of the problem given in Fig. 1. The scattered sound due to the presence of the semi-infinite plate is then computed by

$$p_{s}(\bar{\mathbf{x}},t) = \int_{-\infty}^{\infty} \int_{-\infty}^{\infty} \frac{\partial^{2} T_{ij}(\bar{\mathbf{y}},\tau)}{\partial y_{i} \partial y_{j}} G_{1_{2D}}(\bar{\mathbf{x}},\bar{\mathbf{y}},t-\tau) d^{2}\mathbf{y} d\tau, \tag{4}$$

where  $d^2y$  denotes spatial integration in the plane normal to the plate surface  $(y_1, y_2)$ . The above equation yields the sound scattered by the encounter of a specified turbulence source,  $T_{ij}$ , with the plate edge, which is discussed next.

#### 2.3. Wavepacket source model

We apply a traveling wavepacket model that is based on the model presented by Crighton [16] for the static wavepacket of an axisymmetric free jet. We extend the model to represent a two-dimensional wavepacket (with Gaussian envelopes in both  $y_1$  and  $y_2$  directions) that moves in the  $y_1$  direction with speed  $c_g$ :

$$T_{11}(\bar{\mathbf{y}},\tau) = A e^{i(\omega \tau - k_h y_1)} e^{-\left(\frac{y_1 - c_g \tau}{L_1}\right)^2} e^{-\left(\frac{y_2}{L_2}\right)^2} e^{-\left(\frac{y_1}{L}\right)^2}.$$
 (5)

Here, A is the amplitude of the wavepacket source, which in the case of a source that represents the axisymmetric mode of a jet instability sustains  $A = 2\rho U \tilde{u}$ , where  $\rho$  is the fluid density, U is the exit jet velocity, and  $\tilde{u}$  denotes the axial velocity fluctuations [20]. The amplitude A is arbitrary in the current study, as it has no effect on the directivity of the sound pressure. The length scales  $L_1$  and

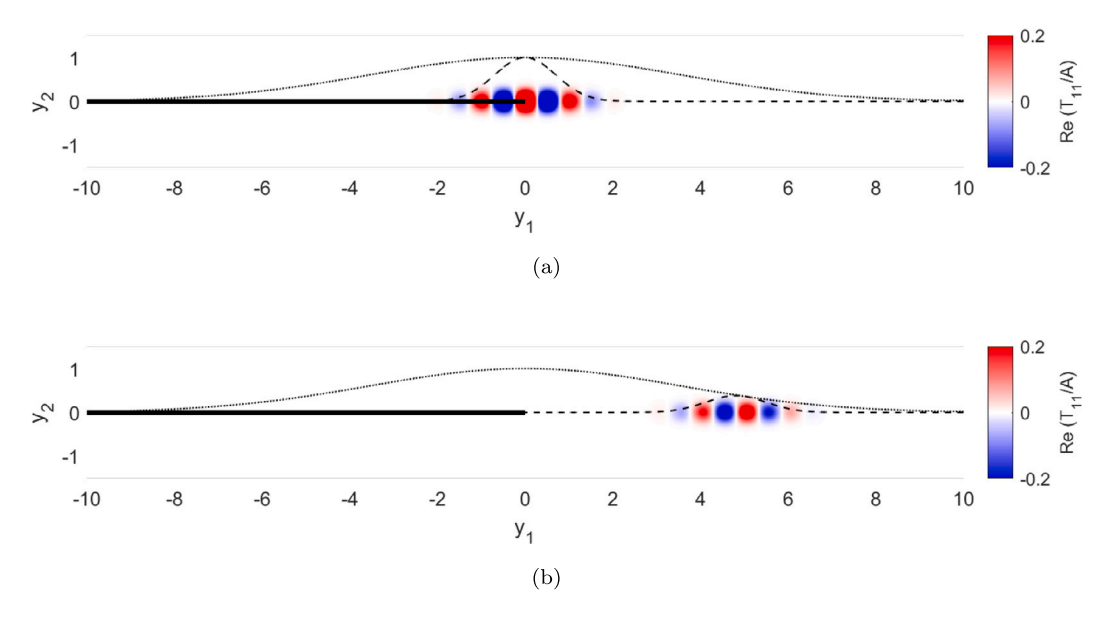


Fig. 2. A wavepacket source model with  $k_h = 6$ ,  $c_g = 1$ ,  $L_1 = 1$ ,  $L_2 = 0.2$ , L = 5 at two different time steps: (a) t = 0; (b) t = 5. Dashed and dotted black curves denote the inside- and outside-envelopes of the wavepacket source in the  $y_1$  direction, respectively. Those envelopes determine the source magnitude as it travels in the  $x_1$  direction, which is denoted by a blue and red color scheme.

 $L_2$  represent the standard deviation of the Gaussian envelopes which are applied in the model in  $y_1$  and  $y_2$  direction, respectively. The additional outer envelope in  $y_1$ , of standard deviation  $L \gg L_1, L_2$ , is added to ensure that the source is localized in the vicinity of the plate edge, and Eq. (4) can be applied to obtain the far field pressure, as suggested by Obrist [27]. In fact, this envelope adds a finite lifespan of approximately  $4L/c_g$  to the source, as demonstrated in Fig. 2. Namely, the observer in the far field will hear a sound for a limited duration.

To study the noise produced by a wavepacket passing the trailing-edge of a semi-infinite plate, we now restrict our analysis to that of a wavepacket that is concentrated on the  $y_2$  axis (i.e., on the plate surface), by applying  $L_2 \to 0$ . We recall that the Dirac delta function can be expressed as

$$\delta(y_2) = \lim_{L_2 \to 0} \left\{ \frac{1}{L_2 \sqrt{\pi}} e^{-\left(\frac{y_2}{L_2}\right)^2} \right\}. \tag{6}$$

Substituting the above relation into Eq. (5) after taking the limit  $L_2 \to 0$  yields a simplified expression for the moving wavepacket line-source.

$$T_{11}(\bar{\mathbf{y}},\tau) \cong A\sqrt{\pi}L_2\,\delta(y_2)\,\mathrm{e}^{f(y_1,\tau)},\tag{7}$$

where

$$f(y_1, \tau) \triangleq i \left(\omega \tau - k_h y_1\right) - \left(\frac{y_1 - c_g \tau}{L_1}\right)^2 - \left(\frac{y_1}{L}\right)^2. \tag{8}$$

With this simplified source model, the second derivative of  $T_{11}$  in space is

$$\frac{\partial^2 T_{11}(\bar{\mathbf{y}},\tau)}{\partial y_1^2} = g(y_1,\tau) \cdot T_{11}(\bar{\mathbf{y}},\tau),\tag{9}$$

where

$$g(y_1, \tau) = \left(2\frac{c_g \tau}{L_1^2} - ik_h\right)^2 - 2\beta^2 - 4\beta^2 \left(2\frac{c_g \tau}{L_1^2} - ik_h\right) y_1 + 4\beta^4 y_1^2,\tag{10}$$

and

$$\beta^2 \triangleq \frac{1}{L_1^2} \left( 1 + \sigma_1^2 \right),\tag{11}$$

where  $\sigma_1 = L_1/L$ . The terms derived in Eqs. (7)–(11) will be applied to Eqs. (1) and (4) to obtain the far-field incident and scattered pressures, respectively.

#### 2.4. Nondimensional variables

A compact representation of the mathematical model is possible with the following choice of nondimensional variables:

$$\hat{t} = t \frac{c_g}{L_1}, \ \lambda = \frac{2\pi}{k_h}, \ \bar{L}_1 = \frac{L_1}{\lambda}, \ R = \frac{r}{L_1}, \ \sigma_1 = \frac{L_1}{L}, \ \sigma_2 = \frac{L_1}{L_2}, \ M_g = \frac{c_g}{c_0}, \ M_c = \frac{k_0}{k_h}, \ k_0 = \frac{\omega}{c_0}, \\ \hat{\boldsymbol{x}} = (\hat{x}_1, \hat{x}_2) = \frac{(x_1, x_2)}{L_1}, \ \hat{\boldsymbol{y}} = (\hat{y}_1, \hat{y}_2) = \frac{(y_1, y_2)}{L_1}.$$
 (12)

Note the use of two separate length scales: the wavepacket length in the  $y_1$  direction,  $L_1$ , is taken as the length scale of the physical problem that normalizes the coordinates and time, while the wavelength of the convected wave,  $\lambda$ , is used to normalize the wavepacket envelope length. This approach is similar to the method presented by Cavalieri et al. [28] in their analysis of the sound engendered by subsonic jets that is modeled as a static wavepacket source, with the exception that their work uses the jet diameter as the physical length scale. In the current study the wavepacket moves along the horizontal axis with group Mach number  $M_g$  and has a convective Mach number  $M_g$ .

Application of the above nondimensional variables to the wavepacket source in Section 2.3 yields

$$T_{11}(\hat{\mathbf{y}},\hat{\tau}) \cong \frac{A\sqrt{\pi}}{\sigma_2} \,\delta(\hat{y}_2) \,\mathrm{e}^{f(\hat{y}_1,\hat{\tau})},\tag{13}$$

where

$$f(\hat{y}_1, \hat{\tau}) = i2\pi \bar{L}_1 \left( \frac{M_c}{M_g} \hat{\tau} - \hat{y}_1 \right) - \left( \hat{y}_1 - \hat{\tau} \right)^2 - \sigma_1^2 \hat{y}_1^2. \tag{14}$$

The second spatial derivative of  $T_{11}$  is then obtained in nondimensional form:

$$\frac{\partial^2 T_{11}(\hat{\mathbf{y}}, \hat{\tau})}{\partial \hat{\mathbf{y}}_1^2} = \hat{g}(\hat{\mathbf{y}}_1, \hat{\tau}) \cdot T_{11}(\hat{\mathbf{y}}, \hat{\tau}),\tag{15}$$

where

$$\hat{g}(\hat{y}_1, \hat{\tau}) = (2\hat{\tau} - i2\pi\bar{L}_1)^2 - 2(1 + \sigma_1^2) - 4(1 + \sigma_1^2)(2\hat{\tau} - i2\pi\bar{L}_1)\hat{y}_1 + 4(1 + \sigma_1^2)^2\hat{y}_1^2.$$
(16)

This concludes the nondimensional representation of the current problem.

#### 2.5. Model limitations

The method of solution presented in Sections. 2.1–2.4 yields the far-field sound produced by a wavepacket that passes near the edge of a semi-infinite plate. Namely, the solution is limited to cases in which the distance between the observer and the edge is much larger than the distance from the wavepacket source to the edge. In addition, the use of the compact Green's function in Section 2.2 implies that the distance between the source and the edge is small compared to the acoustic wavelength,  $\lambda_0$ . In other words we limit our solution to cases of:

$$k_0 r = 2\pi \bar{L}_1 M_c R \gg 1, \tag{17}$$

$$\frac{\lambda_0}{L_1} = \frac{2\pi}{k_0 L_1} = \frac{1}{\bar{L}_1 M_c} \gg |\hat{\mathbf{y}}|,\tag{18}$$

where  $k_0$  is the acoustic wavenumber given in Eq. (12).

## 3. Analytical solution

We next derive an analytical solution based on the formulation of the problem given in Section 2 for two cases: a wavepacket traveling rectilinearly in free space, and a wavepacket that moves along a semi-infinite plate. These solutions yield the incident and scattered pressure fields, respectively, which collectively represent the total sound produced by a wavepacket that passes the edge of a plate. Special consideration is given here to cases where the wavepacket wavenumber is linearly dependent on the location of the wavepacket. This special case is explored to examine the effect of vorticity distortions on the aerodynamic noise, namely to anticipate the effect of relaxing the frozen gust assumption.

### 3.1. Incident field solution

The incident pressure field is obtained by substituting the second spatial derivative of the wavepacket source (Eq. (15)) into Lighthill's integral (Eq. (1)), which yields

$$p_{i}(\hat{\mathbf{x}},\hat{t}) = \frac{A}{4\sigma_{1}\sqrt{\pi}} \int_{-\infty}^{\infty} \frac{L_{1}\delta(\hat{\mathbf{y}}_{2})}{|\hat{\mathbf{x}} - \hat{\mathbf{y}}|} \left[ \hat{g}(\hat{\mathbf{y}}_{1},\hat{\tau}) e^{f(\hat{\mathbf{y}}_{1},\hat{\tau})} \right]_{\hat{\tau} = \hat{t} - M_{g}|\hat{\mathbf{x}} - \hat{\mathbf{y}}|} d^{3}\hat{\mathbf{y}}.$$

$$(19)$$

Focusing on the far field, where  $|\hat{x}| \gg |\hat{y}|$ , a solution for the integral of Eq. (19) is derived by utilizing Howe's far-field approximation (see [25], pp. 20–21), which retains possible phase difference effects, and applying identities (A.2)–(A.4) from Gradshteyn and Ryzhik [29]. This procedure is detailed in Appendix B and leads to a closed form expression for the incident pressure field:

$$p_{i}(\hat{\mathbf{x}},\hat{t}) \cong \frac{A}{4\sigma_{2}\sqrt{-i\bar{L}_{1}M_{c}RF_{2}}} e^{F_{0}-\frac{1}{4}\zeta^{2}} \left\{ \left(E_{0} - \frac{E_{1}}{F_{1}}\right)D_{0}(\zeta) + \left(\frac{E_{2}}{2F_{2}} - \frac{E_{1}}{F_{1}}\right)D_{2}(\zeta) \right\}, \tag{20}$$

where

$$E_0 = 4 \left( t_r - i\pi \bar{L}_1 \right)^2 - 2 \left( 1 + \sigma_1^2 \right), \tag{21}$$

$$E_1 = 8 \left( M_{\sigma} \cos \theta - 1 - \sigma_1^2 \right) \left( t_r - i \pi \bar{L}_1 \right), \tag{22}$$

$$E_2 = 4\left(1 + \sigma_1^2 - M_g \cos\theta\right)^2,\tag{23}$$

$$F_0 = i2\pi \bar{L}_1 \frac{M_c}{M_a} t_r - t_r^2, \tag{24}$$

$$F_1 = -i2\pi \bar{L}_1 \left( 1 - M_c \cos \theta \right) + 2t_r \left( 1 - M_g \cos \theta \right), \tag{25}$$

$$F_2 = -\left(1 - M_a \cos \theta\right)^2 - \sigma_1^2,\tag{26}$$

and  $t_r = \hat{t} - M_g R$  is the retarded time that describes the time at which sound is emitted from the source to reach the observer at the physical time,  $\hat{t}$ . Here  $\zeta^2 = F_1^2/(2F_2)$ , and  $D_v$  are parabolic cylinder functions, which can be expressed in terms of confluent hypergeometric functions (Eq. (A.4)) that are commonly used to describe the solution of the wave equation in paraboloidal coordinates. These functions are useful, for example, in the solution of the Schrödinger equation associated with the hydrogen atom (see Hochstadt [30], pp. 189–195).

We note that for  $c_g \to 0$  we get  $F_1 \sim -i2\pi \bar{L}_1 \left(1 - M_c \cos\theta\right)$ ,  $F_2 \sim -\left(1 + \sigma_1^2\right)$ , and the superdirectivity reported by Cavalieri et al. [18] for a static wavepacket, represented by the exponential function  $\exp\left(1 - M_c \cos\theta\right)^2$ , is reproduced. The full solution for the moving wavepacket includes additional exponential polar variation due to the group velocity (see full expressions given for  $F_1$  and  $F_2$  in Eqs. (25) and (26), respectively) as the location of the wavepacket changes with time.

### 3.2. Scattered field solution

We next utilize the compact Green's function method for computing the sound scattered by a wavepacket passing the edge of a semi-infinite plate. Substitution of Eqs. (2) and (9) into Eq. (4), yields

$$p_s(\hat{\mathbf{x}}, \hat{t}) \cong \frac{AL_2 \sin \frac{\theta}{2}}{\sqrt{\pi r}} \int_{-\infty}^{\infty} \delta(y_2) \, \varphi^*(\bar{\mathbf{y}}) \, \left[ g(y_1, \tau) \, \mathrm{e}^{f(y_1, \tau)} \right]_{\tau = t - \frac{r}{c_0} + \frac{\bar{\mathbf{x}} \cdot \bar{\mathbf{y}}}{c_0}} \, \mathrm{d}^2 \mathbf{y}, \tag{27}$$

where the velocity potential of incompressible flow around the edge of a half-plane,  $\varphi^*(y)$ , satisfies

$$\varphi^*(\mathbf{y}) = \sqrt{r_0} \sin \frac{\theta_0}{2} = \Re \left\{ -i\sqrt{y_1 + iy_2} \right\}. \tag{28}$$

On the plate we obtain

$$\varphi^*(\mathbf{y})\big|_{y_2=0} = \Re\left\{-i\sqrt{y_1}\right\} = \begin{cases} 0, & y_1 > 0, \\ \sqrt{-y_1}, & y_1 < 0. \end{cases}$$
(29)

Substitution of the above expression into Eq. (27) leads to

$$p_s(\hat{\mathbf{x}}, \hat{t}) \cong \frac{A \sin \frac{\theta}{2}}{\sigma_2 \sqrt{\pi R}} e^{F_0} \int_0^\infty \left\{ E_0 \hat{y}_1^{1/2} - E_1 \hat{y}_1^{3/2} + E_2 \hat{y}_1^{5/2} \right\} e^{-F_1 \hat{y}_1 + F_2 \hat{y}_1^2} d\hat{y}_1. \tag{30}$$

Substitutions of the integral identities (A.1) and (A.3) into Eq. (30) leads to a closed-form solution for the scattered pressure field:

$$p_s(\hat{\mathbf{x}}, \hat{t}) \cong \frac{A \sin \frac{\theta}{2}}{2\sigma_2 \left(-2F_2\right)^{3/4} \sqrt{R}} e^{F_0 - \frac{1}{4}\zeta^2} \left\{ \left(E_0 - \frac{3E_1}{2F_1}\right) D_{-\frac{3}{2}} \left(-i\zeta\right) + \frac{15}{4} \left(\frac{E_1}{F_1} - \frac{E_2}{2F_2}\right) D_{-\frac{7}{2}} \left(-i\zeta\right) \right\}. \tag{31}$$

We note that when comparing the above results with the incident field solution (Eq. (20)) the exponential terms are identical, as expected. In addition, the amplitude of the scattered pressure field is proportional to  $\sin\frac{\theta}{2}$ , which is known to control the directivity of the scattering of a point-source from the edge of a semi-infinite plate. However, it is noteworthy that the pressure field dependence on  $\theta$  is also withheld implicitly in the expressions for  $E_1, E_2, F_1$  and  $F_2$  (see Eq. (22), (23), (25), and (26), respectively). This dependence is proportional to  $M_g \cos \theta$  and  $M_c \cos \theta$ , which encompass the effect of the wavepacket group speed and convected wave speed on the scattered sound.

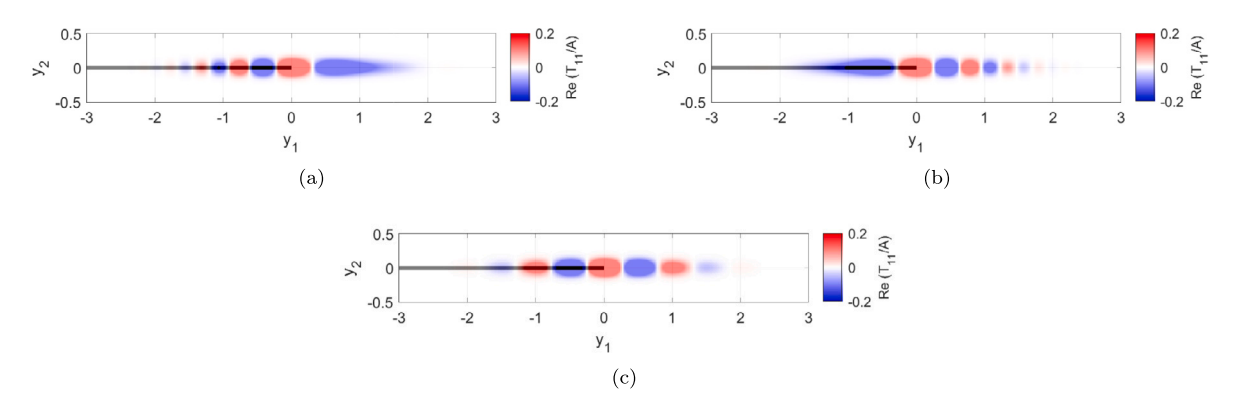


Fig. 3. Wavepacket source models with nominal parameters and three values of linear modification parameters: (a)  $\epsilon = -0.4$ ; (b)  $\epsilon = 0.4$ ; and (c)  $\epsilon = 0$ . Nominal parameters are detailed in Section 4, Table 1.

#### 3.3. Wavenumber modification effect

We next consider a moving wavepacket model in which the wavenumber of the convected wave changes with location  $y_1$ , namely  $k_h = k_h(y_1)$ . Specifically, we assume linear modification of the wavenumber:  $k_h(y_1) = k_{h_0} + ay_1$  where  $|a| \ll k_{h_0}$ , which in nondimensional variables becomes  $k_h L_1 = 2\pi \left(\bar{L}_1 + \epsilon \hat{y}_1\right)$ . Under these conditions the second spatial derivative of the source term is

$$\frac{\partial^2 T_{11}(\hat{\mathbf{y}}, \hat{\boldsymbol{\tau}})}{\partial \hat{\mathbf{y}}_1^2} = \hat{g}_m(\hat{\mathbf{y}}_1, \hat{\boldsymbol{\tau}}) \cdot T_{11}(\hat{\mathbf{y}}, \hat{\boldsymbol{\tau}}), \tag{32}$$

where

$$\begin{split} \hat{g}_{m}(\hat{y}_{1},\hat{\tau}) &= 4\left(\hat{\tau} - i\pi\bar{L}_{1}\right)^{2} - 2\left(1 + \sigma_{1}^{2} + i2\pi\epsilon\right) + 4\hat{y}_{1}^{2}\left(1 + \sigma_{1}^{2} + i2\pi\epsilon\right)^{2} \\ &- 8\left(1 + \sigma_{1}^{2} + i2\pi\epsilon\right)\left(\hat{\tau} - i\pi\bar{L}_{1}\right)\hat{y}_{1}. \end{split} \tag{33}$$

Fig. 3 demonstrates the effect of the wavenumber modification parameter,  $\epsilon$ , on the wavepacket model as it passes the plate edge at time t=0. This model is not intended to represent the exact behavior of the flow near a serrated edge, but rather provide new information on the effect that small local changes in the wavenumber could introduce in the sound produced by the wing trailing edge during flight. We note that the  $\epsilon$  values in Fig. 3 are large for demonstration purposes. In our analysis (Section 4.2) we apply  $\epsilon$  values that are an order of magnitude smaller to sustain the model assumptions  $(|\epsilon| \ll \bar{L}_1)$ .

Application of the modified wavepacket model to the method presented in Section 3.1 (see also Appendix B) leads to modified expressions for the auxiliary Eq. (21)–(23) and (26):

$$E_{m_0} = 4 \left( t_r - i\pi \bar{L}_1 \right)^2 - 2 \left( 1 + \sigma_1^2 + i2\pi\epsilon \right), \tag{34}$$

$$E_{m_1} = 8 \left( M_g \cos \theta - 1 - \sigma_1^2 - i2\pi\epsilon \right) \left( t_r - i\pi \bar{L}_1 \right), \tag{35}$$

$$E_{m_2} = 4\left(1 + \sigma_1^2 + i2\pi\epsilon - M_g \cos\theta\right)^2,\tag{36}$$

$$F_{m_2} = -\left(1 - M_g \cos\theta\right)^2 - \sigma_1^2 - i2\pi\epsilon,\tag{37}$$

while the functions  $F_0$  and  $F_1$  are unaffected by the linear modification in the wavenumber. By applying  $\epsilon \to 0$  to Eqs. (34)–(37) the respective expressions for the constant wavenumber case, Eq. (21)–(23) and (26), are reproduced.

Both the incident and the scattered pressure fields can now be computed by simple replacement of the functions  $E_0$ ,  $E_1$ ,  $E_2$ , and  $F_2$  in the corresponding pressure field expression (Eqs. (20) and (31), respectively) with the modified functions  $E_{m_0}$ ,  $E_{m_1}$ ,  $E_{m_2}$ , and  $F_{m_2}$ . This step closes the formulation of the analytical solution for the sound produced by a wavepacket with a spatially-varying convective wavenumber that passes the edge of a semi-infinite plate.

#### 4. Results

This section presents the pressure field due to a wavepacket passing the edge of a semi-infinite plate for various scenarios of constant or linearly-varying convective wavenumbers. The wavepacket parameters are selected to enable comparison with previous studies of the noise introduced from *static* wavepackets located at specific vertical distances from the plate edge [19,20], as detailed in Table 1. These parameters constitute the nominal case in the following text. As our nondimensional variables do not permit

Table 1
Nominal parameters and their range in the current study.

	$M_c$	$M_{ m g}$	$k_{h_0}L_1$	$\sigma_1$	$\sigma_2$	$\epsilon$	R
Nominal value	0.54	0.01	6	0.1	10	0	35
Examined range	-	0.01-0.54	-	-	-	-0.05 - 0.05	10-50

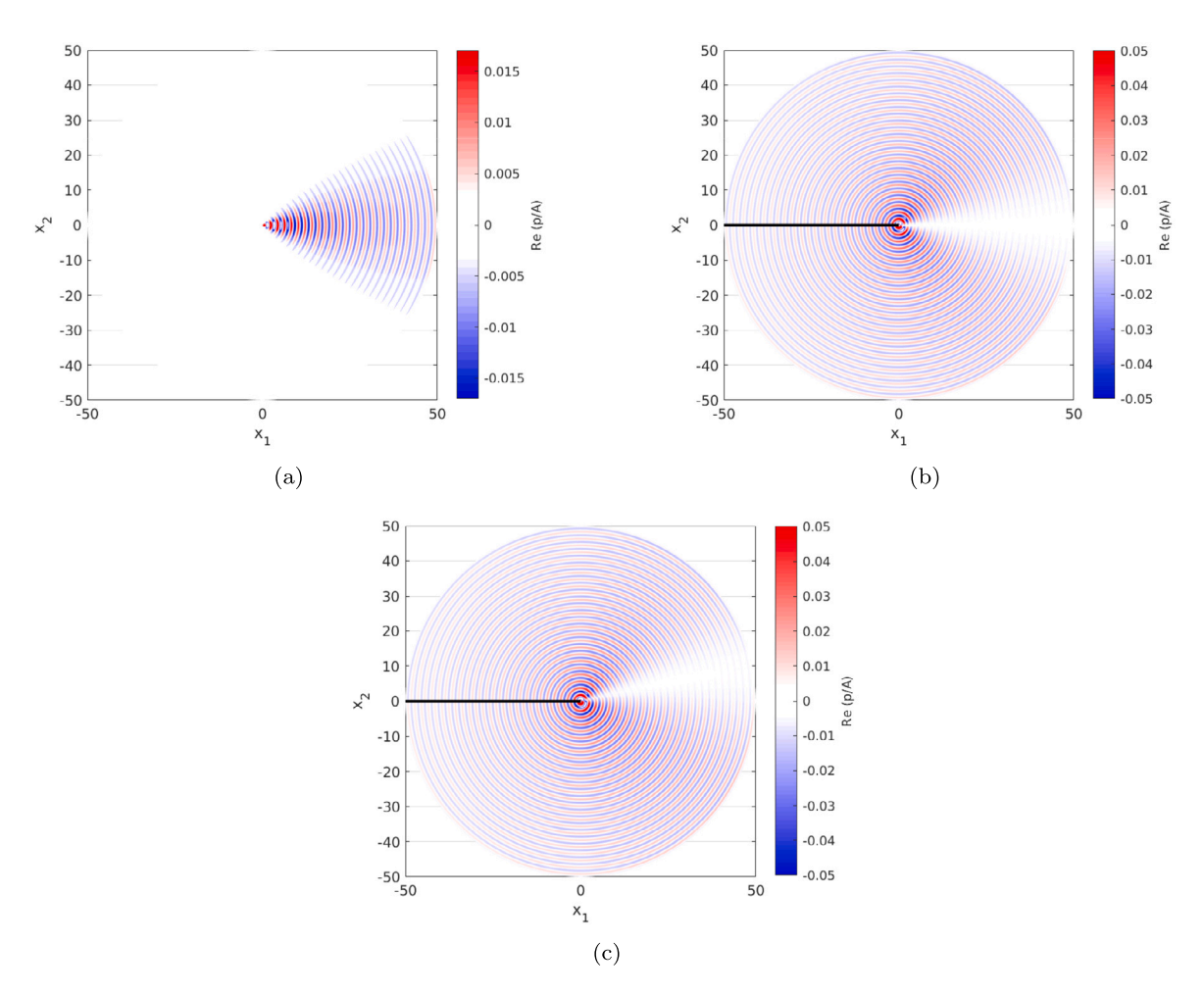


Fig. 4. Real part of the normalized pressure field obtained for a nominal wavepacket source at time t = 0.35: (a) incident field; (b) scattered field; (c) total field. In (b, c) the semi-infinite plate is denoted with a black solid line. Nominal parameters are detailed in Table 1.

the substitution of  $M_g=0$ , a small value of the group Mach number facilitated comparison with the static wavepacket case. In addition, we focus here on small values of  $|t_r|$  for which the wavepacket source remains close to the edge, as required by our model assumptions. A validation of the present analytical model is detailed in Appendix C. For the convenience of the reader the hats above the nondimensional variables are hereafter removed.

#### 4.1. Constant-wavenumber wavepacket: nominal case

Fig. 4 illustrates the far-field acoustic pressure obtained in the incident, scattered, and total fields from a nominal wavepacket source at time t = 0.35. Note that the far-field assumption implies that near-field results in Fig. 4 should be disregarded. Furthermore, our model asserts that the center of the wavepacket reaches the plate edge at time t = 0 and at time t = 0.35 the wavepacket center is located at  $(y_1, y_2) = (0.35, 0)$ , which indicates that the wavepacket still travels along the edge (see Fig. 3(c)) and the disturbance due to this continuous encounter is spread along the field. In both the scattered and the total pressure fields (Figs. 4(b) and 4(c), respectively) a pressure jump is observed between the two sides of the plate, as expected, and the sound is scattered in all directions with an opposite phase between the upper and lower half planes, in agreement with the numerical and experimental results of Cavalieri et al. [19]. In addition, a significant drop in the scattered pressure field is obtained around zero polar angle (Fig. 4(b)), while the incident field is most dominant in the small polar angle regime. The combination of the fields yields the total

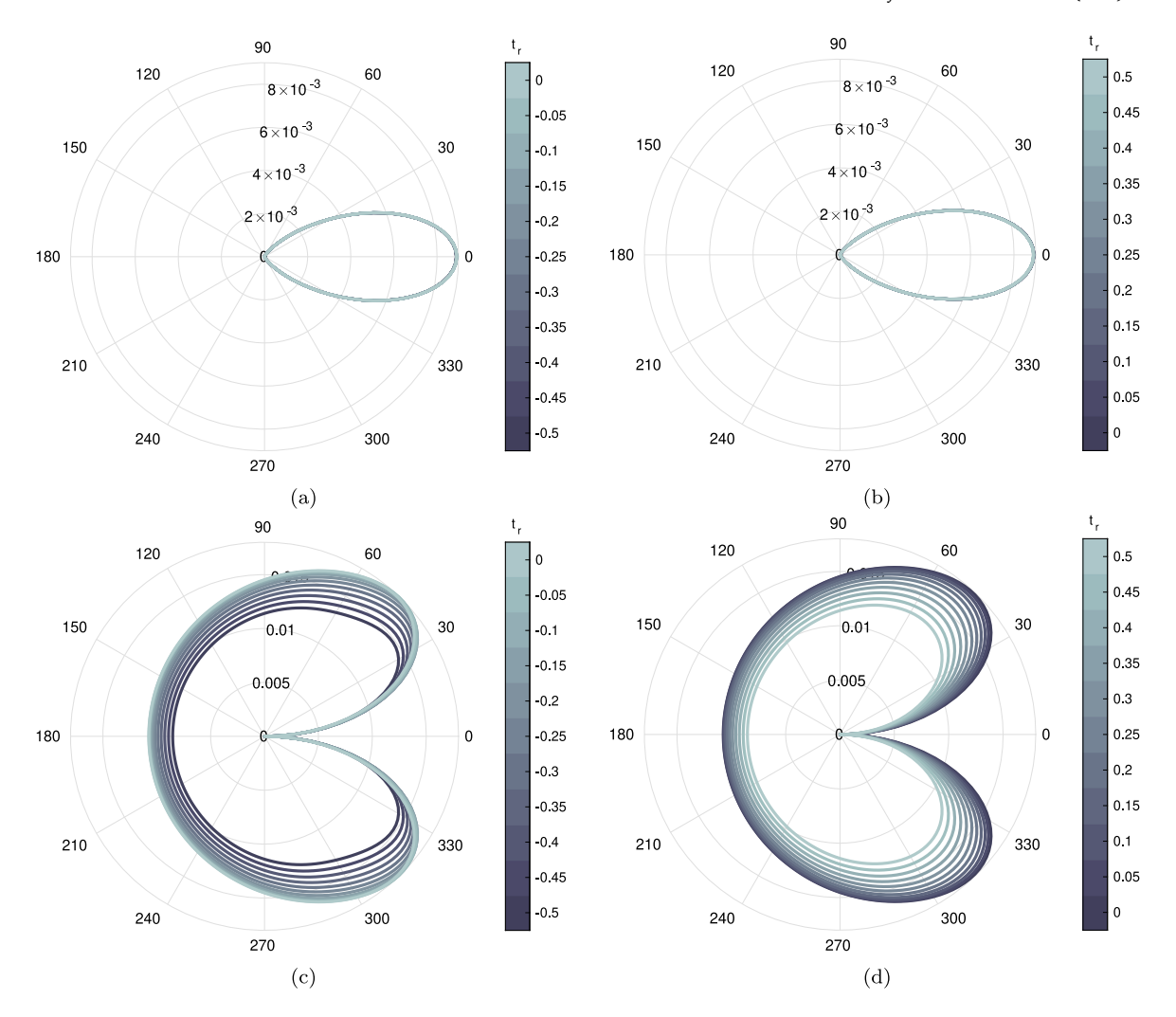


Fig. 5. Polar plot of the normalized pressure amplitude, |p/A|, obtained for a nominal wavepacket source at R = 35 and varying time steps: (a,b) incident field; (c,d) scattered field. Left and right columns present results for  $t_r \le 0$  and  $t_r \ge 0$ , respectively. Nominal parameters are detailed in Table 1.

pressure field in Fig. 4(c), in which a strong drop in pressure is evident around a low polar angle of about 15°. This polar angle in fact depends on the chosen time step, as will be shown next. In general, these pressure fields are in good qualitative agreement with the maps reported by Nogueira et al. [20] for a static wavepacket located below the edge of the plate.

Fig. 5 presents the directivity of the incident and scattered acoustic fields as a function of retarded time. Polar plots of these pressure field amplitudes are obtained for a nominal wavepacket source at a distance R=35 from the origin, and at varying times about  $t_r=0$  (i.e., the instant when the sound produced by a wavepacket that is located at the plate edge reaches the observer). The incident field presented in Figs. 5(a) and 5(b) for  $t_r \le 0$  and  $t_r \ge 0$ , respectively, is practically unaffected by the movement of the wavepacket source, while the maximum incident pressure amplitude is obtained at  $\theta=0^\circ$ , as expected. In contrast, the scattered field in Figs. 5(c) and 5(d) is strongly affected by  $t_r$  and its maximal amplitude is obtained at  $t_r=0$  for a nominal wavepacket source, while the directivity is dominated by the  $\sin\frac{\theta}{2}$  term. As expected, the scattered field amplitude reduces as the distance between the wavepacket and the plate edge increases. In addition, in all of the considered cases both the incident and scattered field amplitudes remain symmetric with respect to the horizontal axis.

The combination of the incident and scattered pressure fields produces the total pressure field presented in Figs. 6(a) and 6(b) for  $t_r \le 0$  and  $t_r \ge 0$ , respectively. The total pressure field results show a distinct dependence on  $t_r$  in the entire polar angle regime. In general, the total pressure amplitude decreases with increased distance between the source and the plate edge for all polar angles except for the small positive angle regime. As both the incident and scattered field amplitudes are practically indifferent to changes in  $t_r$  for small polar angles (Fig. 5), the variation in the total field in this polar angle regime is attributed to the phase difference between both fields. This phase difference is also responsible to the break of symmetry in the total pressure directivity plot, as the symmetry that was evident in the incident and scattered field directivity plots no longer exists in the total field.

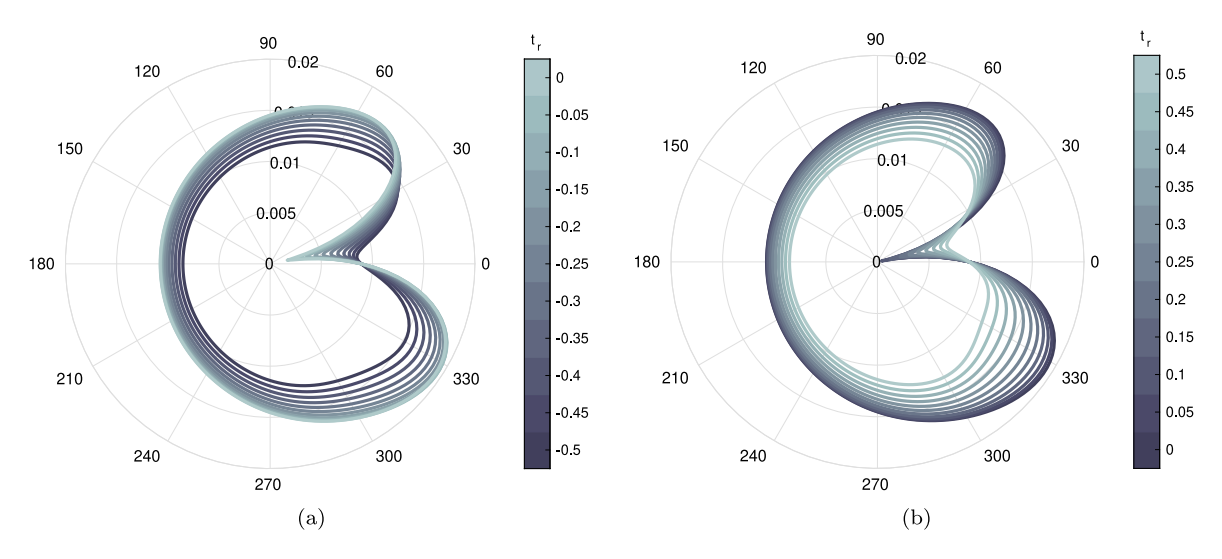


Fig. 6. Polar plot of the normalized total pressure amplitude, |p/A|, obtained for a nominal wavepacket source at R = 35 and varying time steps: (a)  $t_r \le 0$ ; (b)  $t_r \ge 0$ . Nominal parameters are detailed in Table 1.

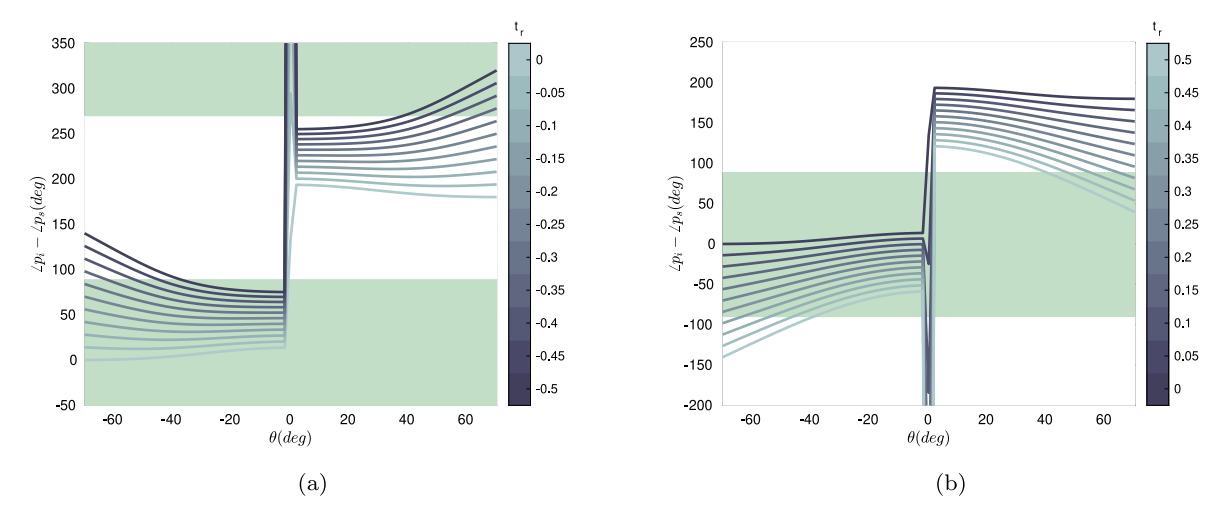
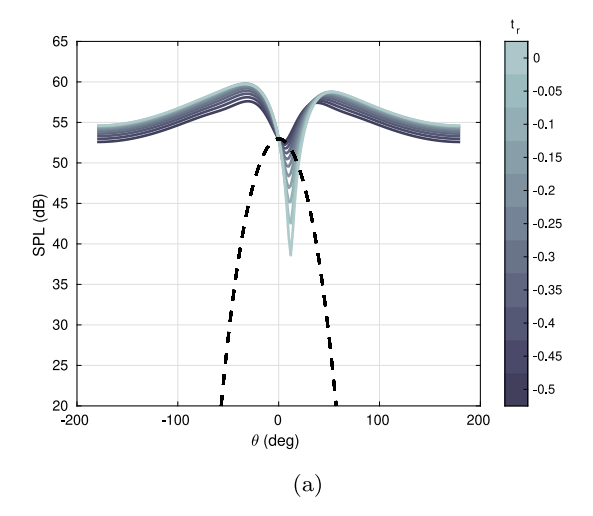


Fig. 7. Phase difference between the incident and scattered fields obtained for a nominal wavepacket source at R = 35 and varying time steps: (a)  $t_r < 0$ ; (b)  $t_r \ge 0$ . Shaded areas identify regions where the total pressure amplitude is larger than the individual field amplitudes in cases in which  $|p_t| \sim |p_s|$ . Nominal parameters are detailed in Table 1.

Figs. 7(a) and 7(b) present this phase difference for  $t_r \le 0$  and  $t_r \ge 0$ , respectively, in which the shaded areas denote phase difference angles that are in the right half plane. These shaded regions identify cases in which the total amplitude is larger than the scattered field amplitude when  $|p_t| \sim |p_s|$ , while white areas denote regions where the amplitude of the total field is small compared to the individual fields. In general, for small negative polar angles the phase difference angle is in the right half plane, while for low positive polar angles the phase difference angle is in the left half plane, which reduces the total amplitude. Therefore, the symmetric shape of the scattered field becomes asymmetric in the total field plot with decreased amplitude in the low positive polar angles region and increased amplitude at small negative polar angles (Fig. 6). This asymmetry is reduced as the distance between the wavepacket source and the plate edge increases (i.e., as  $|t_r|$  increases).

The appropriate SPL distribution is presented in Figs. 8(a) and 8(b) for a nominal wavepacket source at negative and positive values of  $t_r$ , respectively. At large values of  $|\theta|$  the sound level reduces with increase in the distance between the wavepacket and the edge, as expected, while for small polar angles a region of reduced sound level relative to that of the incident field is observed. Both of these trends bear resemblance to the results reported by Cavalieri et al. [19] in their Figure 13a, where they used the method of Ffowcs Williams and Hall [21] to compute the sound from a static wavepacket placed in different vertical locations under the plate edge. However, Cavalieri et al. [19] focused on cases where the distance between the wavepacket and the edge is  $\mathcal{O}(1)$ , and not small as considered here. Further details on the comparison between the current solution and the results obtained by Cavalieri et al. [19] are available in Appendix C.



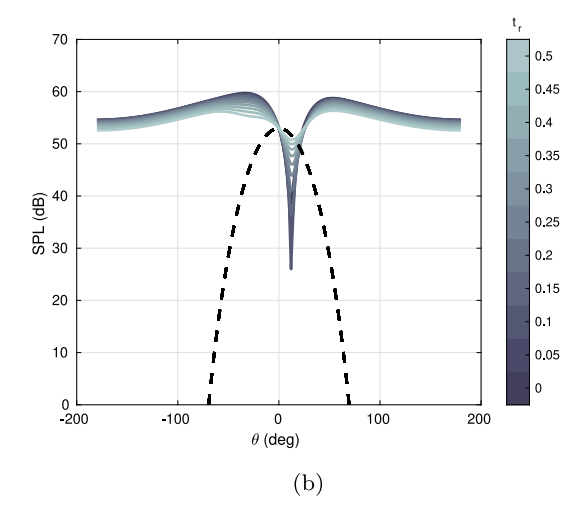


Fig. 8. SPL obtained for a nominal wavepacket source at R = 35 and varying time steps: (a)  $t_r \le 0$ ; (b)  $t_r \ge 0$ . Dashed black lines denote the appropriate SPL distribution of the incident field. SPL is calculated for the normalized pressure field, relative to a reference pressure of  $p_{ref}/A = 2 \cdot 10^{-5}$ . Nominal parameters are detailed in Table 1.

#### 4.2. Spatially-varying wavepackets

The above results for the nominal case were obtained for a wavepacket of constant wavenumber ( $\epsilon = 0$ ). The effect of loosening this constraint is examined next in Fig. 9, where the incident and scattered pressure amplitudes are presented for varying values of the wavenumber modification parameter. The incident field presented in Figs. 9(a) and 9(b) for  $\epsilon = -0.01$  and  $\epsilon = 0.01$ , respectively, is clearly affected by the modification parameter, where the pressure amplitude increases with a decrease in the wavenumber. However, the scattered pressure field in Fig. 9(c) is practically unaffected by this modification for the case considered. The total pressure amplitudes computed for  $\epsilon = -0.01, 0, 0.01$  are presented in Fig. 9(d), where it is clear that the wavenumber modification affects the small polar angles regime and has less impact on the large polar angle regime where the scattered field is most dominant.

To further explore the effect of the linear wavenumber modification on the pressure amplitude, Fig. 10 shows the results obtained for the nominal case parameters used in Fig. 9, computed for a specific retarded time of  $t_r = 0.5$  and a wide range of  $\epsilon$ . We note a similarity to the cases of varying retarded time plotted in Fig. 9: an increase in  $\epsilon$  while  $t_r$  is kept constant leads to a decrease in the incident field amplitude while only slightly affecting the scattered field. However, when combining the separate fields to obtain the total pressure field amplitude (Fig. 10(c)), the effect of the wavepacket modification is not limited to small polar angles of, say,  $-30^{\circ} \le \theta \le 30^{\circ}$  where the incident field amplitude is most dominant, but rather this effect is expanded to angles of  $-60^{\circ} \le \theta \le 60^{\circ}$  which must be related to the phase difference between the scattered and incident fields. This phase difference, plotted in Fig. 10(d), is in fact negative for  $\theta < 0^{\circ}$  and positive for  $\theta > 0^{\circ}$  with a 180° jump at  $\theta = 0^{\circ}$ . We further note that when the phase difference represents an angle in the left half plane (white areas in Fig. 10(d)) and the individual field amplitudes are of the same order of magnitude, the total pressure amplitude will be reduced compared to the scattered contribution alone, as is confirmed in Fig. 10(c). These phase differences also explain the asymmetry that is evident in the total pressure amplitude relative to  $\theta = 0^{\circ}$ , although the incident and scattered field amplitudes are each symmetric in  $\theta$ .

## 4.3. Parametric investigation of the group mach number effect

Fig. 11 presents the effect that variation in the group Mach number has on the incident, scattered, and total pressure field amplitudes for a nominal wavepacket that moves at speeds between  $M_g=0.05M_c$  and  $M_g=M_c$ . Similarly to the effect of the modification parameter,  $\epsilon$ , presented in Fig. 10, variations in  $M_g$  only affect the amplitude of the incident field in any practical sense, while the scattered field amplitude remains virtually unchanged. As a result, the total pressure amplitude is only affected by  $M_g$  at small polar angles of  $-30^{\circ} \le \theta \le 30^{\circ}$ . In addition, the effect of  $M_g$  is only evident in the total pressure amplitude obtained with low Mach numbers of  $M_g < 0.35M_c$ , as higher group Mach numbers yield a very low-amplitude incident field such that the scattered field controls the total pressure field for all  $\theta$  except  $\theta = 0^{\circ}$ .

Fig. 12 presents the effect of linear variation in the wavepacket wavenumber on the total pressure field obtained for cases where the wavepacket is moving with  $M_g$  between  $0.1M_c$  and  $0.4M_c$ . As is expected from Fig. 11(a), the incident field is most dominant for the lower values of  $M_g$ , and as the group Mach number is increased the effect of  $\epsilon$  diminishes in the low polar angles regime. In general, negative values of  $\epsilon$  have the strongest effect on the far-field pressure amplitude computed at  $t_r = 0.5$ , as these values in fact reduce the wavenumber behind the edge, which is equivalent to increasing the convective Mach number while keeping the group Mach number constant. Namely, a negative  $\epsilon$  is analogous to a local decrease in the ratio  $M_g/M_c$ . These negative values of  $\epsilon$  amplify the total pressure field for low polar angles where the incident field is most dominant, whereas for moderate polar angles

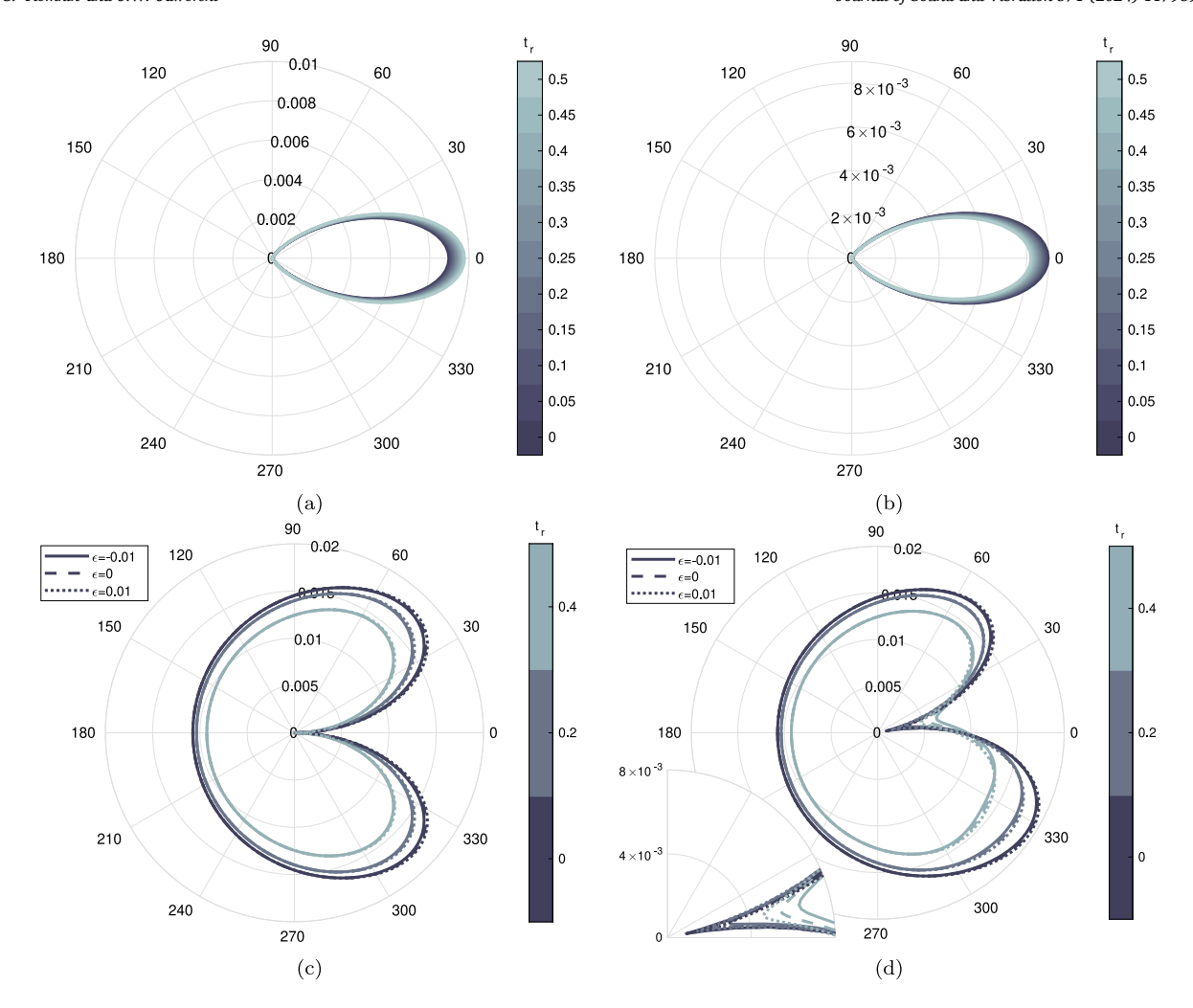


Fig. 9. Polar plot of the normalized pressure amplitude, |p/A|, obtained for a wavepacket source of nominal parameters and various values of the wavenumber modification,  $\epsilon$ : (a) incident field with  $\epsilon = -0.01$ ; (b) incident field with  $\epsilon = 0.01$ ; (c) scattered field obtained with  $\epsilon = -0.01, 0.0.01$ ; (d) total field obtained with  $\epsilon = -0.01, 0.0.01$ . Results are presented for R = 35 and retarded time  $t_r \ge 0$ , when the wavepacket passes the plate edge. Nominal parameters are detailed in Table 1.

the phase difference between the incident and scattered fields leads to amplification of the pressure amplitude in the upper half plane and reduction in amplitude for the lower half plane (see discussion above on the phase difference in Fig. 10(d)). As  $M_g/M_c$  increases, the effect of the incident field reduces; however, the asymmetric contribution of the phase difference is still clearly evident for negative values of  $\epsilon$ .

## 5. Concluding remarks

An analytical model is developed to predict the sound produced by a wavepacket moving past the edge of a semi-infinite flat plate. Closed-form expressions for the incident and scattered acoustic fields are obtained in the time domain for traveling wavepackets with constant or spatially-varying wavenumbers. The solution for a spatial variation in the wavepacket wavenumber enables the effect of relaxing the frozen gust assumption for theoretical edge-noise prediction to be examined for the first time.

Analytical results for a wavepacket of constant wavenumber moving with very low velocity ( $M_{\rm g}=0.01$ ) show good qualitative agreement with numerical results presented by Cavalieri et al. [19] for a *static* wavepacket positioned at various vertical distances under the plate edge. The speed of the wavepacket, as described parametrically by the group Mach number, affects the incident field amplitude but has no significant effect on the amplitude of the scattered field. Thus, the total pressure field is parametrically affected by changes in the incident field amplitude and the phase difference between the incident and scattered fields.

An extension of the analytical solution to model linear spatial variations in the wavepacket wavenumber serves as a surrogate model to study the effect of turbulence distortions, which are known to occur for example near serrated trailing edges (e.g., Avallone et al. [13]), on the far-field sound. However, we focus on the effect of the vorticity distortion by separating it from the effect of

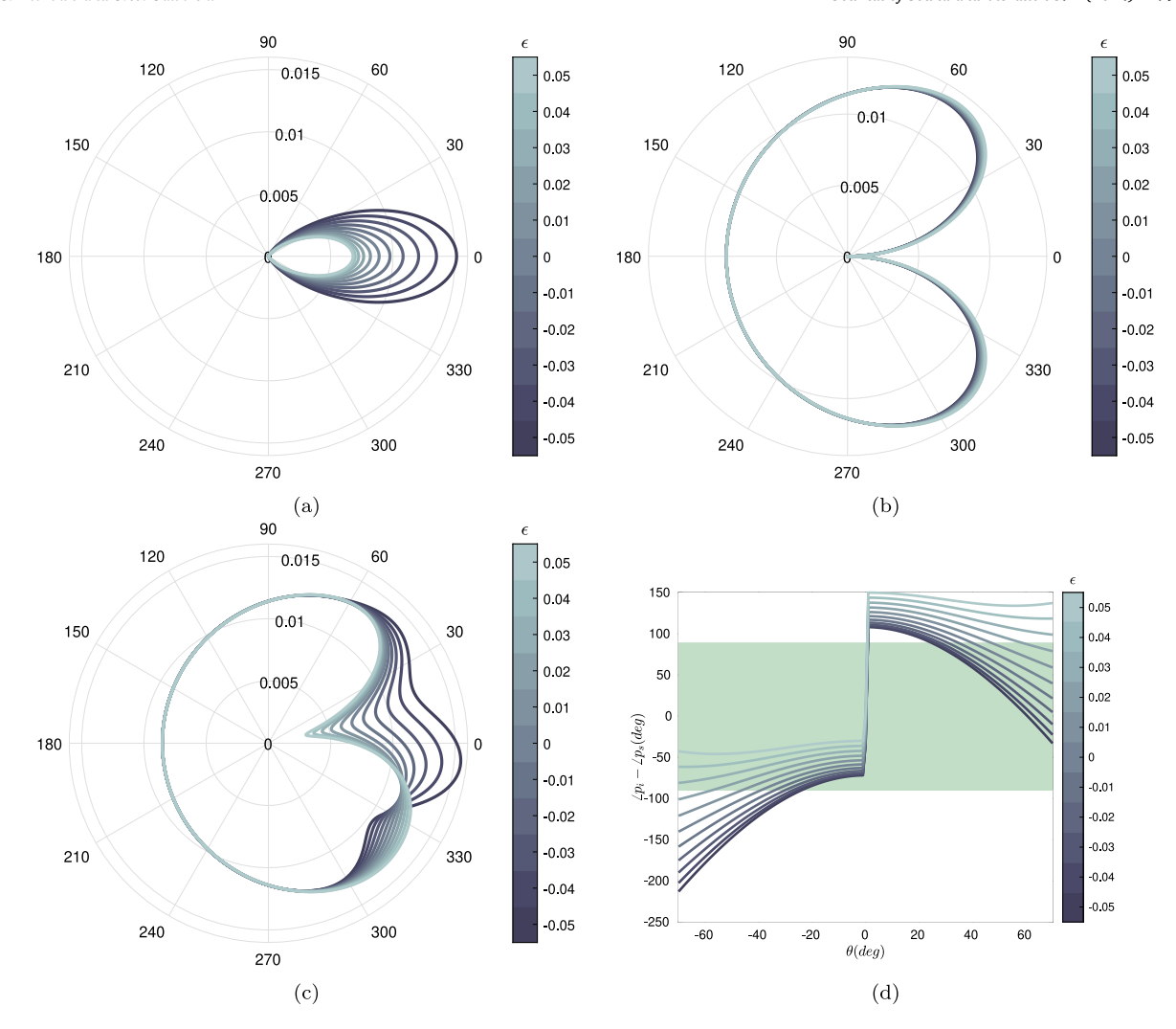


Fig. 10. Polar plot of the normalized pressure amplitude, |p/A|, obtained for a wavepacket source of nominal parameters and varying values of  $\epsilon$ : (a) incident field; (b) scattered field; (c) total field; (d) phase difference between incident and scattered fields. Results are presented for R=35 and retarded time  $t_r=0.5$ , after the wavepacket passed the plate edge. Shaded area in (d) identifies the regions where the total pressure amplitude is larger than the individual field amplitudes in cases in which  $|p_t| \sim |p_s|$ . Nominal parameters are detailed in Table 1.

trailing edge geometry and solving the problem for a straight trailing edge. Closed-form analytical expressions are derived for the far-field acoustic pressure in cases of linear wavenumber modification, where the parabolic cylinder functions play a key role; note that the analytical formulation derived here could also be applied to other prescribed spatial wavenumber variations. Our results show that a linear modification in the wavepacket wavenumber affects mainly the incident field amplitude, whereas the scattered field amplitude is practically unaffected by the wavenumber modification parameter,  $\epsilon$ . However, the phase difference between the incident and scattered fields is strongly affected by  $\epsilon$ , and therefore the total pressure amplitude is altered beyond the region dominated by the incident field.

This work reveals that vorticity distortions in the vicinity of the wing trailing edge may have very little influence on the scattered pressure amplitude, while significantly affecting the total pressure field through its effect on the incident field amplitude and the phase difference between both fields. Further extension of the current model to realistic distortions in the vorticity fields, based on computational or experimental results, are expected to yield further scientific understanding of the role of the frozen gust assumption (or its violation) in the sound radiated from a trailing edge. Such an extension invites a numerical investigation that could present a wide parametric analysis to which the current closed-form expressions could serve as verification points. Further advancement could also be achieved by combining the current model with a novel analytical Green's function that describes the serrated-edge scattering (e.g., Lyu [31]). This combined model could reveal the role of the frozen gust assumption in the acoustic scattering of serrated edges, and expose the reasons for current disagreement between theoretical and computational or experimental studies of the sound produced by a geometrically-varying trailing edge.

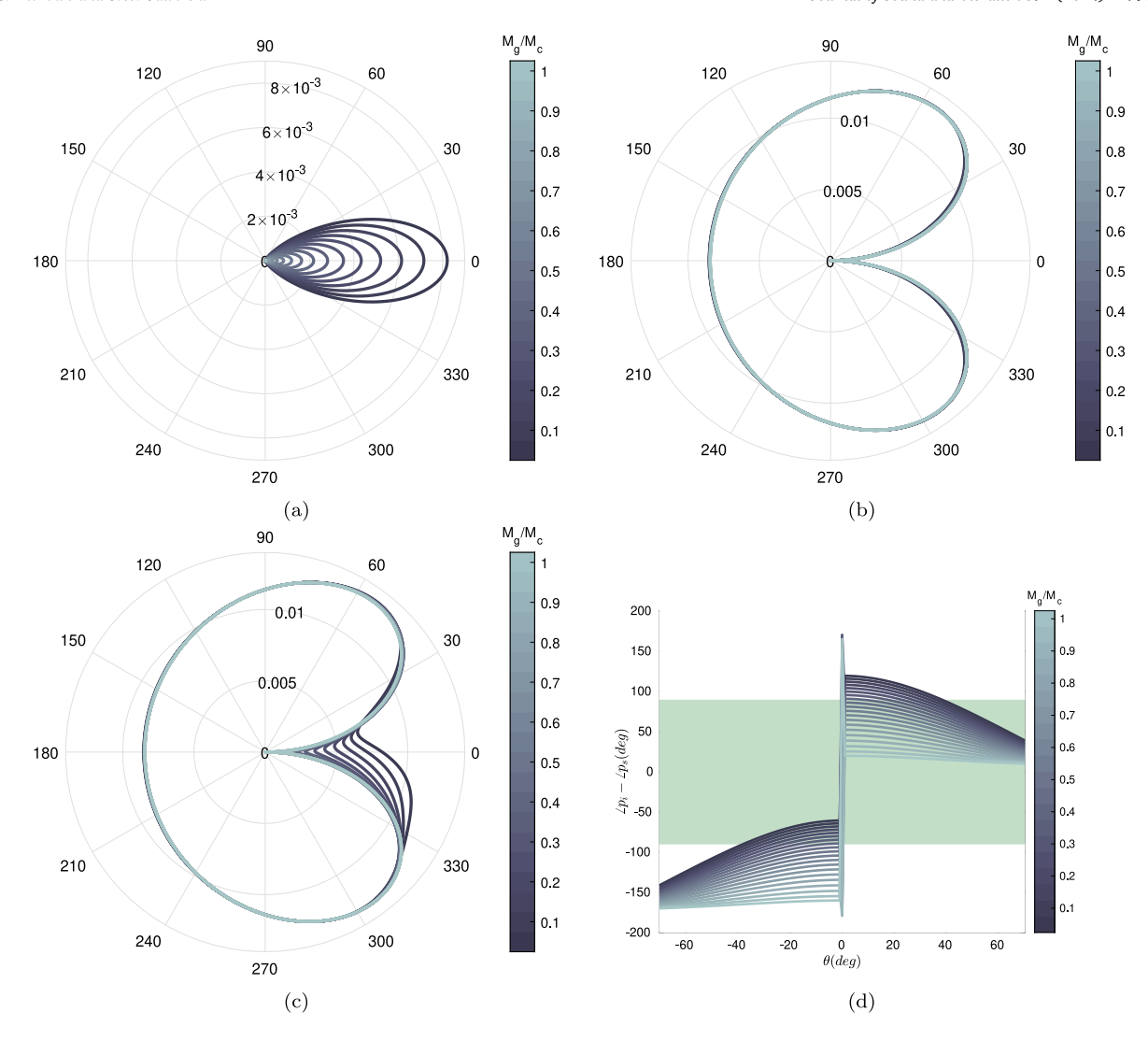


Fig. 11. Polar plot of the normalized pressure amplitude, |p/A|, obtained for a wavepacket source of nominal parameters and varying values of  $M_g$ : (a) incident field; (b) scattered field; (c) total field; (d) phase difference between incident and scattered fields. Results are presented for R = 35 and retarded time  $t_r = 0.5$ , after the wavepacket passed the plate edge. Shaded area in (d) identifies the regions where the total pressure amplitude is larger than the individual field amplitudes in cases in which  $|p_t| \sim |p_s|$ . Nominal parameters are detailed in Table 1.

#### CRediT authorship contribution statement

**Sonya Tiomkin:** Methodology, Validation, Formal analysis, Writing – original draft, Visualization. **Justin W. Jaworski:** Conceptualization, Funding acquisition, Writing – review & editing.

## Declaration of competing interest

The authors declare that they have no known competing financial interests or personal relationships that could have appeared to influence the work reported in this paper.

#### Data availability

No data was used for the research described in the article

#### Acknowledgment

This work was supported by the National Science Foundation, USA under award 1846852, with partial support from the Zuckerman-CHE STEM Leadership Program (Israel).

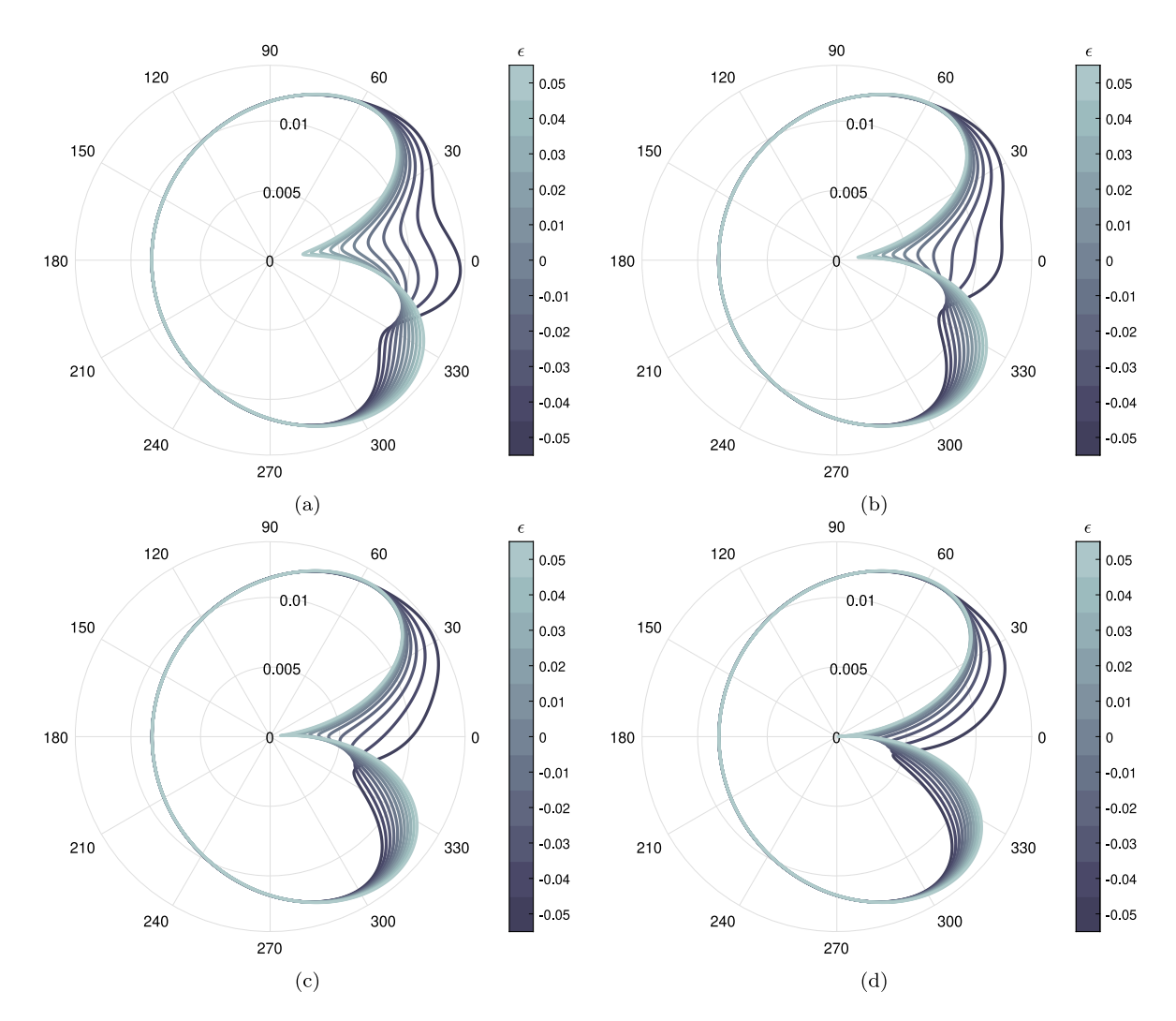


Fig. 12. Polar plot of the total pressure amplitude obtained for a wavepacket source of nominal parameters for varying values of  $\epsilon$  and four values of  $M_g$ : (a)  $M_g = 0.1 M_c$ ; (b)  $M_g = 0.2 M_c$ ; (c)  $M_g = 0.3 M_c$ ; (d)  $M_g = 0.4 M_c$ . Results are presented for R = 35 and retarded time  $t_r = 0.5$ , after the wavepacket passed the plate edge. Nominal parameters are detailed in Table 1.

## Appendix A. Mathematical identities

The following identities appear in [29] as Eqs. 3.462(1), 3.462(3), 9.247(1), and 9.24, respectively, and are used in the derivations of Section 3:

$$\int_{0}^{\infty} x^{\nu - 1} e^{-\beta x^{2} - \gamma x} dx = (2\beta)^{-\nu/2} \Gamma(\nu) e^{\frac{\gamma^{2}}{8\beta}} D_{-\nu} \left( \frac{\gamma}{\sqrt{2\beta}} \right), \tag{A.1}$$

where  $D_{-\nu}$  are parabolic cylinder functions,  $\Gamma$  is the Gamma function, and  $\Re\left\{\beta\right\}>0, \Re\left\{\nu\right\}>0$ .

$$\int_{-\infty}^{\infty} (ix)^{\nu} e^{-\beta^{2} x^{2} - iqx} dx = 2^{-\nu/2} \sqrt{\pi} \beta^{-\nu - 1} e^{-\frac{q^{2}}{8\beta^{2}}} D_{\nu} \left( \frac{q}{\beta \sqrt{2}} \right), \tag{A.2}$$

where  $\Re \{\beta\} > 0, \Re \{\nu\} > -1, \Im \{x\} = 0.$ 

$$D_{\nu+1}(z) - zD_{\nu}(z) + \nu D_{\nu-1}(z) = 0. \tag{A.3}$$

$$D_{v}(z) = 2^{\frac{1}{4} + \frac{v}{2}} \, W_{\frac{1}{4} + \frac{v}{2}, -\frac{1}{4}} \left( \frac{z^2}{2} \right) \, z^{-\frac{1}{2}}$$

$$=2^{\frac{\nu}{2}}e^{-\frac{1}{4}z^{2}}\left\{\frac{\sqrt{\pi}}{\Gamma(\frac{1-\nu}{2})}\boldsymbol{\Phi}\left(-\frac{\nu}{2},\frac{1}{2};\frac{1}{2}z^{2}\right)-\frac{\sqrt{2\pi}z}{\Gamma(-\frac{\nu}{2})}\boldsymbol{\Phi}\left(-\frac{1-\nu}{2},\frac{3}{2};\frac{1}{2}z^{2}\right)\right\}$$
(A.4)

where  $W_{\xi,\mu}\left(\frac{1}{2}\xi^2\right)$  is the Whittaker function, and  $\Phi(\alpha,\gamma;z)$  is the confluent hypergeometric function. Our numerical validation (Appendix C) revealed that the above relation between the parabolic cylinder functions and the Whittaker functions is not valid for cases in which both  $\nu$  and z are negative. Therefore, in the Matlab presentation of the analytical solutions we utilize the second equivalence in Eq. (A.4), where the parabolic cylinder functions are expressed in terms of the confluent hypergeometric functions.

#### Appendix B. Derivation of the incident pressure field

This appendix details the derivation of the closed-form expression for the incident field, given by Eq. (20). We begin by evaluating the integral of Eq. (19) in  $y_3$ . We are interested in the far-field solution,  $|\mathbf{x}| \gg |\mathbf{y}|$ , so we can define:  $\hat{\mathbf{x}} = (\hat{x}_1, \hat{x}_2), \hat{\mathbf{y}} = (\hat{y}_1, \hat{y}_2), \hat{\xi} = \hat{y}_3 - \hat{x}_3$ , and  $R = \sqrt{\hat{x}_1^2 + \hat{x}_2^2} \gg |\hat{\mathbf{y}}|$ , which leads to

$$|\tilde{\mathbf{x}} - \tilde{\mathbf{y}}| \cong R\sqrt{1 + \mu^2} - \frac{\hat{y}_1 \cos \theta + \hat{y}_2 \sin \theta}{\sqrt{1 + \mu^2}},\tag{B.1}$$

$$\frac{1}{|\tilde{\mathbf{x}} - \tilde{\mathbf{y}}|} \cong \frac{1}{R\sqrt{1 + \mu^2}},\tag{B.2}$$

where  $\mu = \hat{\xi}/R$ , and  $\tilde{x} = x/L_1$  and  $\tilde{y} = y/L_1$  are the normalized three-dimensional spacial coordinate vectors. This approximation follows the method of Howe [25, pp. 20–21], to retain possible phase difference effects in the far-field solution. We can now continue to solve the integral

$$I_3 \triangleq \int_{-\infty}^{\infty} \left[ \frac{\hat{g}(\hat{y}_1, \hat{\tau})}{|\tilde{x} - \tilde{y}|} e^{f(\hat{y}_1, \hat{\tau})} \right] d\hat{y}_3, \tag{B.3}$$

where the square brackets denote retarded time,  $\hat{\tau} = \hat{t} - M_g |\tilde{x} - \tilde{y}|$ , such that

$$\begin{split} \left[ \hat{g}(\hat{y}_{1}, \hat{\tau}) \right] &\cong \left( 2\hat{i} - 2M_{g}R\sqrt{1 + \mu^{2}} + \frac{2M_{g}\left(\hat{y}_{1}\cos\theta + \hat{y}_{2}\sin\theta\right)}{\sqrt{1 + \mu^{2}}} - i2\pi\bar{L}_{1} \right)^{2} \\ &- 4(1 + \sigma_{1}^{2}) \left( 2\hat{i} - 2M_{g}R\sqrt{1 + \mu^{2}} + \frac{2M_{g}\left(\hat{y}_{1}\cos\theta + \hat{y}_{2}\sin\theta\right)}{\sqrt{1 + \mu^{2}}} - i2\pi\bar{L}_{1} \right) \hat{y}_{1} \\ &- 2(1 + \sigma_{1}^{2}) + 4(1 + \sigma_{1}^{2})^{2} \hat{y}_{1}^{2}, \end{split} \tag{B.4}$$

and

$$\begin{split} \left[ f(\hat{y}_{1}, \hat{\tau}) \right] &\cong i2\pi \bar{L}_{1} \left( \frac{M_{c}}{M_{g}} \hat{t} - M_{c} R \sqrt{1 + \mu^{2}} + \frac{M_{c} \left( \hat{y}_{1} \cos \theta + \hat{y}_{2} \sin \theta \right)}{\sqrt{1 + \mu^{2}}} - \hat{y}_{1} \right) \\ &- \left( \hat{t} - M_{g} R \sqrt{1 + \mu^{2}} + \frac{M_{g} \left( \hat{y}_{1} \cos \theta + \hat{y}_{2} \sin \theta \right)}{\sqrt{1 + \mu^{2}}} - \hat{y}_{1} \right)^{2} - \sigma_{1}^{2} \hat{y}_{1}^{2}. \end{split} \tag{B.5}$$

We note that  $k_0r \to \infty$  ( $M_cR \to \infty$ ) for the far-field solution, and the exponent in the integrand of  $I_3$  oscillates increasingly rapidly, as seen from the imaginary part of  $[f(y_1, \tau)]$  (first term in Eq. (B.5)). The exponential amplitude, which is equivalent to the exponent of the real part of  $[f(y_1, \tau)]$  (second and third terms in Eq. (B.5)) is finite, as evident by the negative value of  $\Re[f(y_1, \tau)]$ . We thus conclude that the main contribution to the  $I_3$  integral comes from the vicinity of  $\mu = 0$ , where stationary oscillations are obtained. In other words, the stationary phase method is applied to Eq. (B.3) for  $M_cR \to \infty$ , yielding

$$I_{3} \cong \int_{-\infty}^{\infty} \left[ \frac{\hat{g}(\hat{y}_{1}, \hat{\tau})}{\sqrt{1 + \mu^{2}}} e^{f(\hat{y}_{1}, \hat{\tau})} \right] d\mu \cong e^{i2\pi \bar{L}_{1} \left( \frac{M_{c}}{M_{g}} \hat{\iota} - \hat{y}_{1} \right) - (t_{r} + M_{g}(\hat{y}_{1} \cos \theta + \hat{y}_{2} \sin \theta) - \hat{y}_{1})^{2} - \sigma_{1}^{2} \hat{y}_{1}^{2}} \cdot \left[ \hat{g}(\hat{y}_{1}, \hat{\tau}) \right]_{\mu=0} \int_{-\infty}^{\infty} e^{-i2\pi \bar{L}_{1} M_{c} R \left( \sqrt{1 + \mu^{2}} - \frac{\hat{y}_{1} \cos \theta + \hat{y}_{2} \sin \theta}{R \sqrt{1 + \mu^{2}}} \right)} d\mu,$$
(B.6)

where  $t_r = \hat{t} - M_{\sigma}R$ , and

$$\int_{-\infty}^{\infty} e^{-i2\pi \bar{L}_1 M_c R \left( \sqrt{1+\mu^2} - \frac{\hat{y}_1 \cos \theta + \hat{y}_2 \sin \theta}{R\sqrt{1+\mu^2}} \right)} d\mu \cong \sqrt{\frac{1}{i\bar{L}_1 M_c R}} e^{-i2\pi \bar{L}_1 M_c R \left( 1 - \frac{\hat{y}_1 \cos \theta + \hat{y}_2 \sin \theta}{R} \right)}.$$
(B.7)

Applying the above result to Eq. (B.6) yields

$$I_{3} \cong \sqrt{\frac{1}{\mathrm{i}\bar{L}_{1}M_{c}R}} \left[ \hat{g}(\hat{y}_{1},\hat{\tau}) \right]_{\mu=0} \mathrm{e}^{\mathrm{i}2\pi\bar{L}_{1} \left( \frac{M_{c}}{M_{g}} t_{r} - \hat{y}_{1}(1-M_{c}\cos\theta) + \hat{y}_{2}M_{c}\sin\theta \right) - \left( t_{r} - \hat{y}_{1}\left( 1-M_{g}\cos\theta \right) + \hat{y}_{2}M_{g}\sin\theta \right)^{2} - \sigma_{1}^{2}\hat{y}_{1}^{2}}. \tag{B.8}$$

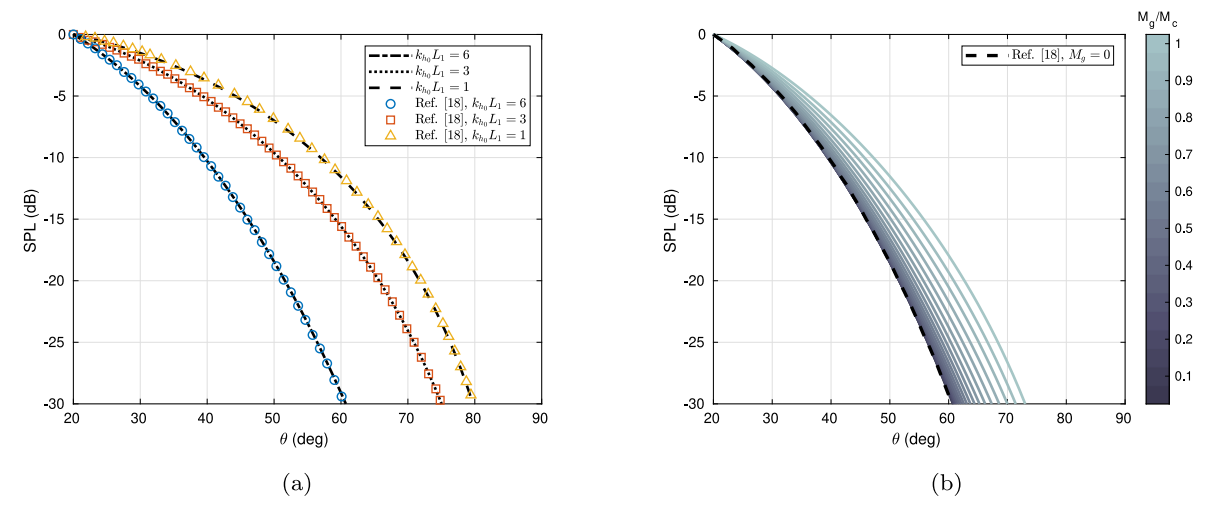


Fig. C.1. SPL distribution obtained for the incident field and compared against the results of Cavalieri et al. [18] for a wavepacket source of  $M_c = 0.36$ , R = 35,  $\epsilon = 0$ : (a)  $k_{h_0}L_1 = 1, 3, 6$ ,  $M_g = 0.01$ ; (b)  $k_{h_0}L_1 = 6$  and  $M_g$  varies. Good agreement is obtained between [18] and the current solution as  $M_g \to 0$ . Values at  $\theta = 20^\circ$  are fixed at 0 dB.

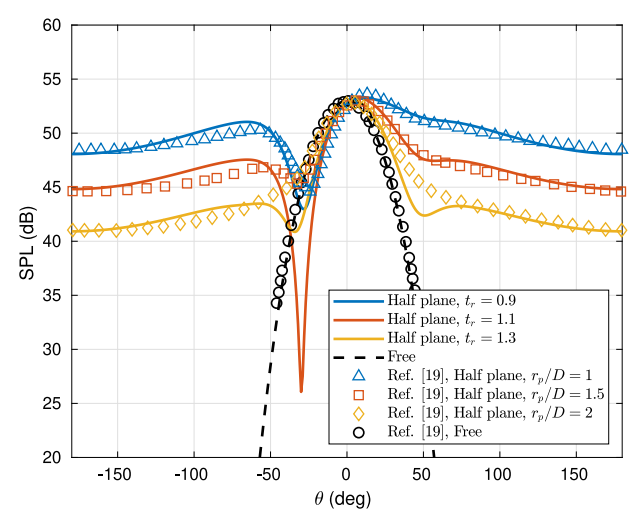


Fig. C.2. SPL distribution of the incident and total fields obtained for a wavepacket source of  $M_c = 0.54$ , R = 35,  $k_{h_0}L_1 = 6$ ,  $\epsilon = 0$ , and  $M_g = 0.01$ . Results of the current solution are presented with solid lines for three different time steps:  $t_r = 0.9, 1.1, 1.3$ , which represent moments when the wavepacket have passed the plate edge, and compared against the results of Cavalieri et al. [19] obtained for a static wavepacket located at a distance of  $r_p/D = 1, 1.5, 2$  beneath the plate edge, where D is the jet diameter and  $r_p$  is a radial distance between the jet axis and the plate edge. The SPL values from Cavalieri et al. [19] were shifted downward by 50 dB for comparison with the current model. This shift has no effect on the directivity of the distribution.

Substitution of Eq. (B.8) into the pressure field expression in Eq. (19) yields

$$p_{i}(\hat{\mathbf{x}},\hat{t}) \cong \frac{A}{4\sigma_{2}\sqrt{\mathrm{i}\pi\bar{L}_{1}M_{c}R}} e^{F_{0}} \int_{-\infty}^{\infty} \left\{ E_{0} + E_{1}\hat{y}_{1} + E_{2}\hat{y}_{1}^{2} \right\} e^{F_{1}\hat{y}_{1} + F_{2}\hat{y}_{1}^{2}} \mathrm{d}\hat{y}_{1}, \tag{B.9}$$

where

$$\left[\hat{g}(\hat{y}_1, \hat{\tau})\right]_{\substack{\mu=0\\y_2=0}} \triangleq E_0 + E_1 \hat{y}_1 + E_2 \hat{y}_1^2, \tag{B.10}$$

and the expressions for  $E_0, E_1, E_2, F_0, F_1$ , and  $F_2$  are given in Eqs. (21)–(26), respectively.

Eq. (B.9) is solved by applying the integral identities given in Eqs. (A.2) and (A.3), which leads to the closed-form expression in Eq. (20).

#### Appendix C. Validation of solution

This appendix presents a validation analysis for the analytical solutions presented in Eqs. (20) and (31) for the incident and scattered fields, respectively. Validation of the incident field results is first sought through comparison of the SPL directivity obtained

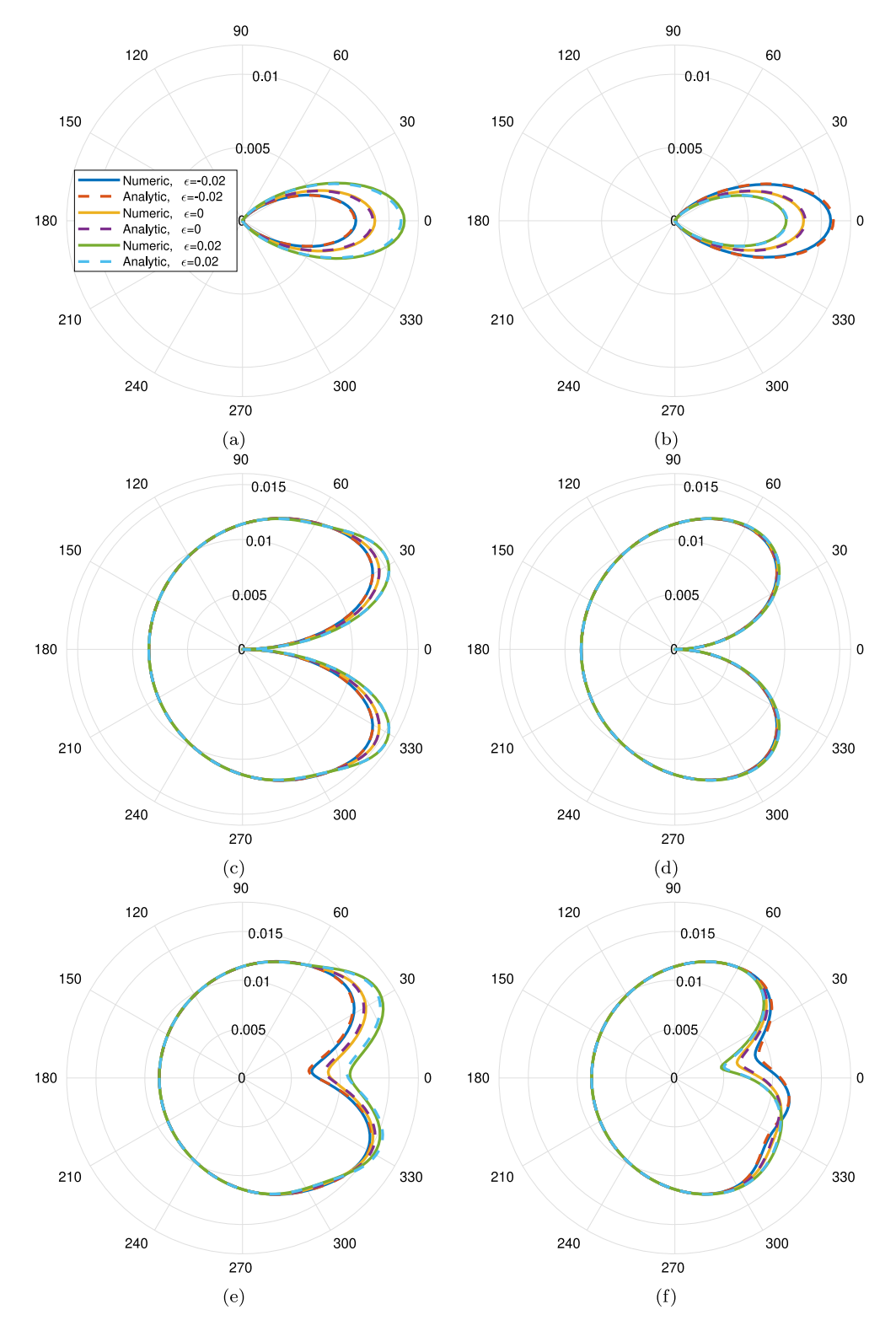


Fig. C.3. Numerical validation of the analytical expressions obtained for (a, b) the incident field, (c, d) the scattered field, and (e, f) the total field, for a nominal wavepacket source with  $\epsilon = -0.02, 0, 0.02$ , at a distance R = 35 and retarded time  $t_r = -0.5$  (left column) and  $t_r = 0.5$  (right column).

in the current study with the results that Cavalieri et al. [18] obtained for a *static* line-source wavepacket model of  $M_c = 0.36$ , at R = 35, using three different values of  $k_{h_0}L_1$  (Fig. C.1(a)). The comparison is achieved by applying  $M_g = 0.01$  to the current *moving* wavepacket model and focusing on retarded time  $t_r = 0$ , when the sound produced by a wavepacket that is located at the axis origin reaches the observer. The SPL values at  $\theta = 20^\circ$  are fixed at 0 dB in Fig. C.1, following the convention in [18]. The current results agree well with the results of [18] for all of the examined cases. In addition, variation in the group Mach number seems to affect the  $\theta$  range in which the sound is radiated, with that range reducing to lower angles as  $M_g \to 0$  and converging to the static solution of [18] (see Fig. C.1(b)), as expected. The good agreement between the current solution, obtained for  $M_g = 0.01$ , and the results of Cavalieri et al. [18] validate the expressions derived for the incident field in Section 3.1.

A similar validation of the analytical solution obtained for the sound generated by a wavepacket that passes the edge of a semiinfinite plate is sought through comparison of the total SPL distribution obtained with the analytical solutions derived in Section 3, and the numerical solutions of Cavalieri et al. [19] and Nogueira et al. [20] for a static wavepacket model. Fig. C.2 presents the total SPL field obtained with the current analytical solution for three different time steps:  $t_r = 0.9, 1.1, 1.3$  for a wavepacket model of  $M_c = 0.54$ , R = 35,  $k_{h_0}L_1 = 6$ ,  $\epsilon = 0$ , and  $M_g = 0.01$ . These time-steps were chosen as they presented the best fit with the results reported by [19] for a static wavepacket located at a distance of  $r_p/D = 1, 1.5, 2$  beneath the plate edge, where D is the jet diameter and r<sub>n</sub> denotes radial distance from the jet axis. For the sake of comparison, the SPL plots of Cavalieri et al. [19] were shifted downward by 50 dB to fit the current results. This shift has no effect on the directivity of the solutions. In fact, the directivity of the present results shows good agreement with the results of [19] in the upper half plane ( $\theta > 0^{\circ}$ ), more so for cases in which the wavepacket is closer to the edge. In the lower half plane the agreement is not as good as the differences in the models are more significant there. Indeed, Cavalieri et al. [19] have applied a volume wavepacket source to represent the axisymmetric mode of a subsonic jet positioned below the edge of a plate. This model was later simplified by Nogueira et al. [20] as a cylindrical surface along the jet lipline with no evident effect on the radiated sound. In contrast, the current study applies a line-source wavepacket that moves along the plate axis. Therefore, for a very close distance between the wavepacket and the edge a good agreement is expected with [19,20], whereas for larger distances the differences between the models are expected to play a bigger role, especially in the lower half-plane where stronger sound reflections are expected in the cases where the wavepacket is underneath the plate edge. This is indeed the case shown in Fig. C.2.

The above results show qualitative validation of the current solution through comparison with previous computational studies of various wavepacket models. Further quantitative validation of the analytical expressions presented in Section 3 is next pursued by comparing the closed form expressions in Eqs. (20) and (31), with the appropriate numerical solution of Eq. (19) (after substitution of Eqs. (B.3) and (B.6)) and (27), respectively. Fig. C.3 presents the results of this comparison for the nominal parameters described in Table 1, at two retarded time steps ( $t_r = \pm 0.5$ ) and for three different values of linear modification in the wavenumber,  $\epsilon = -0.02, 0, 0.02$ . Very good agreement between the numerical and analytical solutions of the incident, scattered, and total fields is observed in all of the considered cases, validating the novel analytical expressions of Section 3.

#### References

- [1] S. Karabasov, L.J. Ayton, X. Wu, M. Afsar, Advances in aeroacoustics research: Recent developments and perspectives, Phil. Trans. R. Soc. A 377 (2159) (2019) 20190390.
- [2] D.P. Thipphavong, R. Apaza, B. Barmore, V. Battiste, B. Burian, Q. Dao, M. Feary, S. Go, K.H. Goodrich, J. Homola, et al., Urban air mobility airspace integration concepts and considerations, in: 2018 Aviation Technology, Integration, and Operations Conference, Paper AIAA-2018-3676, Atlanta, Georgia, 2018
- [3] T.F. Brooks, D.S. Pope, M.A. Marcolini, Airfoil Self-Noise and Prediction, NASA Technical Report 1218, 1989.
- [4] A.S. Hersh, P.T. Soderman, R.E. Hayden, Investigation of acoustic effects of leading-edge serrations on airfoils, J. Aircr. 11 (4) (1974) 197-202.
- [5] J.W. Jaworski, N. Peake, Aeroacoustics of silent owl flight, Annu. Rev. Fluid Mech. 52 (1) (2020) 395-420.
- [6] M.S. Howe, Noise produced by a sawtooth trailing edge, J. Acoust. Soc. Am. 90 (1) (1991) 482-487.
- [7] M.S. Howe, Aerodynamic noise of a serrated trailing edge, J. Fluids Struct. 5 (1) (1991) 33–45.
- [8] L.J. Ayton, Analytic solution for aerodynamic noise generated by plates with spanwise-varying trailing edges, J. Fluid Mech. 849 (2018) 448-466.
- [9] D.J. Moreau, C.J. Doolan, Noise-reduction mechanism of a flat-plate serrated trailing edge, AIAA J. 51 (10) (2013) 2513-2522.
- [10] F. Avallone, W.C.P. van der Velden, D. Ragni, D. Casalino, Noise reduction mechanisms of sawtooth and combed-sawtooth trailing-edge serrations, J. Fluid Mech. 848 (2018) 560–591.
- [11] M. Gruber, P. Joseph, T.P. Chong, Experimental investigation of airfoil self noise and turbulent wake reduction by the use of trailing edge serrations, in: 16th AIAA/CEAS Aeroacoustics Conference, Paper AIAA-2018-3803, Stockholm, Sweden, 2010.
- [12] T.F. Brooks, T.H. Hodgson, Trailing edge noise prediction from measured surface pressures, J. Sound Vib. 78 (1) (1981) 69–117.
- [13] F. Avallone, S. Pröbsting, D. Ragni, Three-dimensional flow field over a trailing-edge serration and implications on broadband noise, Phys. Fluids 28 (11) (2016) 117101.
- [14] S. Lee, L. Ayton, F. Bertagnolio, S. Moreau, T.P. Chong, P. Joseph, Turbulent boundary layer trailing-edge noise: Theory, computation, experiment, and application, Prog. Aerosp. Sci. 126 (2021) 100737.
- [15] S.C. Crow, Acoustic gain of a turbulent jet, Paper IE.6, in: Meeting of Division of Fluid Dynamics, American Physical Society, University of Colorado, Boulder, 1972.
- [16] D.G. Crighton, Basic principles of aerodynamic noise generation, Prog. Aerosp. Sci. 16 (1) (1975) 31-96.
- [17] D.G. Crighton, P. Huerre, Shear-layer pressure fluctuations and superdirective acoustic sources, J. Fluid Mech. 220 (1990) 355-368.
- [18] A.V.G. Cavalieri, P. Jordan, T. Colonius, Y. Gervais, Axisymmetric superdirectivity in subsonic jets, J. Fluid Mech. 704 (2012) 388-420.
- [19] A.V.G. Cavalieri, P. Jordan, W.R. Wolf, Y. Gervais, Scattering of wavepackets by a flat plate in the vicinity of a turbulent jet, J. Sound Vib. 333 (24) (2014) 6516-6531.
- [20] P.A.S. Nogueira, A.V.G. Cavalieri, P. Jordan, A model problem for sound radiation by an installed jet, J. Sound Vib. 391 (2017) 95-115.
- [21] J.E.F. Williams, L.H. Hall, Aerodynamic sound generation by turbulent flow in the vicinity of a scattering half plane, J. Fluid Mech. 40 (4) (1970) 657–670.
- [22] W.R. Wolf, S.K. Lele, Wideband fast multipole boundary element method: Application to acoustic scattering from aerodynamic bodies, Internat. J. Numer. Methods Fluids 67 (12) (2011) 2108–2129.

- [23] A.V.G. Cavalieri, W.R. Wolf, J.W. Jaworski, Numerical solution of acoustic scattering by finite perforated elastic plates, Proc. R. Soc. Lond. Ser. A Math. Phys. Eng. Sci. 472 (2188) (2016) 20150767.
- [24] L.J. Ayton, M.J. Colbrook, T.F. Geyer, P. Chaitanya, E. Sarradj, Reducing aerofoil-turbulence interaction noise through chordwise-varying porosity, J. Fluid Mech. 906 (2021) A1.
- [25] M.S. Howe, Theory of Vortex Sound, Cambridge University Press, United Kingdom, 2003.
- [26] M.S. Howe, Contributions to the theory of aerodynamic sound, with application to excess jet noise and the theory of the flute, J. Fluid Mech. 71 (4) (1975) 625-673.
- [27] D. Obrist, Acoustic emissions from convected wave packets, Phys. Fluids 23 (2) (2011) 026101.
- [28] A.V.G. Cavalieri, P. Jordan, A. Agarwal, Y. Gervais, Jittering wave-packet models for subsonic jet noise, J. Sound Vib. 330 (18) (2011) 4474-4492.
- [29] I.S. Gradshteyn, I.M. Ryzhik, Table of Integrals, Series, and Products, fifth ed., Academic Press, United States of America, 1994,
- [30] H. Hochstadt, The Functions of Mathematical Physics, Dover, New York, 1986.
- [31] B. Lyu, Analytical Green's function for the acoustic scattering by a flat plate with a serrated edge, J. Fluid Mech. 961 (2023) A33.